ATMAD : robust image analysis for Automatic Tissue MicroArray De-arraying

Hoaï-Nam Nguyen, Vincent Paveau, Cyril Cauchois, Charles Kervrann

ATMAD : robust image analysis for Automatic Tissue MicroArray De-arraying [1]

Hoai-Nam Nguyen[1], **Vincent Paveau**[2], **Cyril Cauchois**[2], **Charles Kervrann**[1]

[1] Inria, Centre Rennes-Bretagne Atlantique, SERPICO Project Team, 35042 Rennes, France

[2] Innopsys Inc., Carbonne 31390, France

Background. Over the last two decades, an innovative technology called Tissue Microarray (TMA), which combines multi-tissue and DNA microarray concepts, has been widely used in the field of histology. It consists of a collection of several (up to 1000 or more) tissue samples that are assembled onto a single support – typically a glass slide – according to a design grid (array) layout, in order to allow multiplex analysis by treating numerous samples under identical and standardized conditions. However, during the TMA manufacturing process, the sample positions can be highly distorted from the design grid due to the imprecision when assembling tissue samples and the deformation of the embedding waxes. Consequently, these distortions may lead to severe errors of (histological) assay results when the sample identities are mismatched between the design and its manufactured output. The development of a robust method for de-arraying TMA, which localizes and matches TMA samples with their design grid, is therefore crucial to overcome the bottleneck of this prominent technology.

Results. In this paper, we propose an Automatic, fast and robust TMA De-arraying (ATMAD) approach dedicated to images acquired with bright field and fluorescence microscopes (or scanners). First, tissue samples are localized in the large image by applying a locally adaptive thresholding on the isotropic wavelet transform of the input TMA image. To reduce false detections, a parametric shape model is considered for segmenting ellipse-shaped objects at each detected position. Segmented objects that do not meet the size and the roundness criteria are discarded from the list of tissue samples before being matched with the design grid. Sample matching is performed by estimating the TMA grid deformation under the thin-plate model. Finally, thanks to the estimated deformation, the true tissue samples that were preliminary rejected in the early image processing step are recognized by running a second segmentation step.

Conclusions. We developed a novel de-arraying approach for TMA analysis. By combining wavelet-based detection, active contour segmentation, and thin-plate spline interpolation, our approach is able to handle TMA images with high dynamic, poor signal-to-noise ratio, complex background and non-linear deformation of TMA grid. In addition, the deformation estimation produces quantitative information to asset the manufacturing quality of TMAs.

Keywords : tissue microarray, TMA de-arraying, detection, wavelet, segmentation, active contour, deformation, thin-plate spline

1. This work was supported by Innopsys Inc.

1 Background

1.1 Tissue MicroArrays (TMA) history

The development of multi-tissue techniques was started at the mid-1980s in order to address the scarcity issue of diagnostic reagents and tissue samples. The pioneer work was contributed by Dr Battifora who introduced, in 1986, the multi-tumor "sausage" tissue block [1]. In this method, several rods of tissue, which were extracted from paraffin-embedded tissue blocks (or shortened as paraffin blocks), deparaffinized and rehydrated, were put together and reparaffinized after being tightly wrapped in small intestine of small mammals like a sausage. To avoid deparaffinization and reparaffinization procedures of Battifora's "sausage" technique, in 1987, Wan *et al.* conceived the punching technique [2] which used 16-gauge needle for retrieving cylinders of tissue (also tissue cores) from paraffin blocks and arraying them in a recognizable pattern. Although Wan's punching technique was a big footstep and was used in nearly all of today TMA techniques, its tissue pattern was not a grid one which is more structured and facilitates the identification of each tissue sample. The first multi-tissue grid pattern is described by Battifora and Mehta in their 1990's paper under the name of "checkerboard tissue block" [3] in which tissue rods were manually aligned in a Cartesian coordinate system (checkerboard pattern). By combining the punching technique of Wan and the "checkerboard" concept of Battifora and Mehta, Kononen *et al.* invented in 1998 a machine for assembling efficiently and accurately extracted tissue cores in grid pattern [4]. The proposed technique called "tissue microarray" (TMA) became therefore popular and widely used in most pathological laboratories. In the last decade, different TMA techniques were developed to improve manufacturing process and minimize manufacturing cost [5, 6, 7, 8, 9, 10, 11, 12, 13, 14, 15], but all of them were based on Battifora's, Wan's and Kononen's previous works. Since in most TMA techniques, extracted tissue samples have cylinder form, in the following, we use the terms "tissue cores" or "TMA cores" (or even more shorter cores) to refer TMA tissue samples.

1.2 Challenges of TMA de-arraying

In a TMA, assembled tissue cores are collected from different donor blocks. It is thus highly important to matching them with their proper meta-data for further clinical or pathological analysis. To this end, grid pattern was conceived to ease the localization of each TMA cores. However, in spite of numerous technique improvements [12, 16], TMAs manufactured recently by manual or automated (semi-automated) machine are still subjected to the deformation of the design tissue grid due to bad positioning of the tissue cores with respect to the design. Another main source of deformation is the heat deformation of the paraffin waxes – commonly used in TMA techniques – when embedding tissue cores into recipient block. Sectioning paraffin-embedded tissue blocks with a microtome to produce multiple slides may also produce additional deformation. In fact, the design grid may suffer geometric transformations such as translation, rotation and shearing (linear or affine deformations) combined with dilatation, distortion and random perturbations (non-linear deformations). In addition, some fragile tissue cores may be lost or split into several fragmented parts, making more difficulties to recognize them. Figure 1 illustrates a typical image of TMA imaged in fluorescence. We can clearly observed that the ideal TMA grid which is a square grid is significantly distorted after the manufacturing process and the present tissue cores do not have a perfectly circular shape as expected. These problems need to be taken into account to develop robust de-arraying methods.

FIGURE 1 – **Deformation of the TMA grid.** An ideal TMA (left top) has tissue cores perfectly aligned in vertical and horizontal directions with equal spacing according to a regular square grid (left bottom). The manufactured TMA (right top) is subjected to a non-linear deformation of the TMA grid resulting to a distorted grid (right bottom). We aim at de-arraying the observed TMA by estimating the deformation which transforms the ideal grid into the distorted grid.

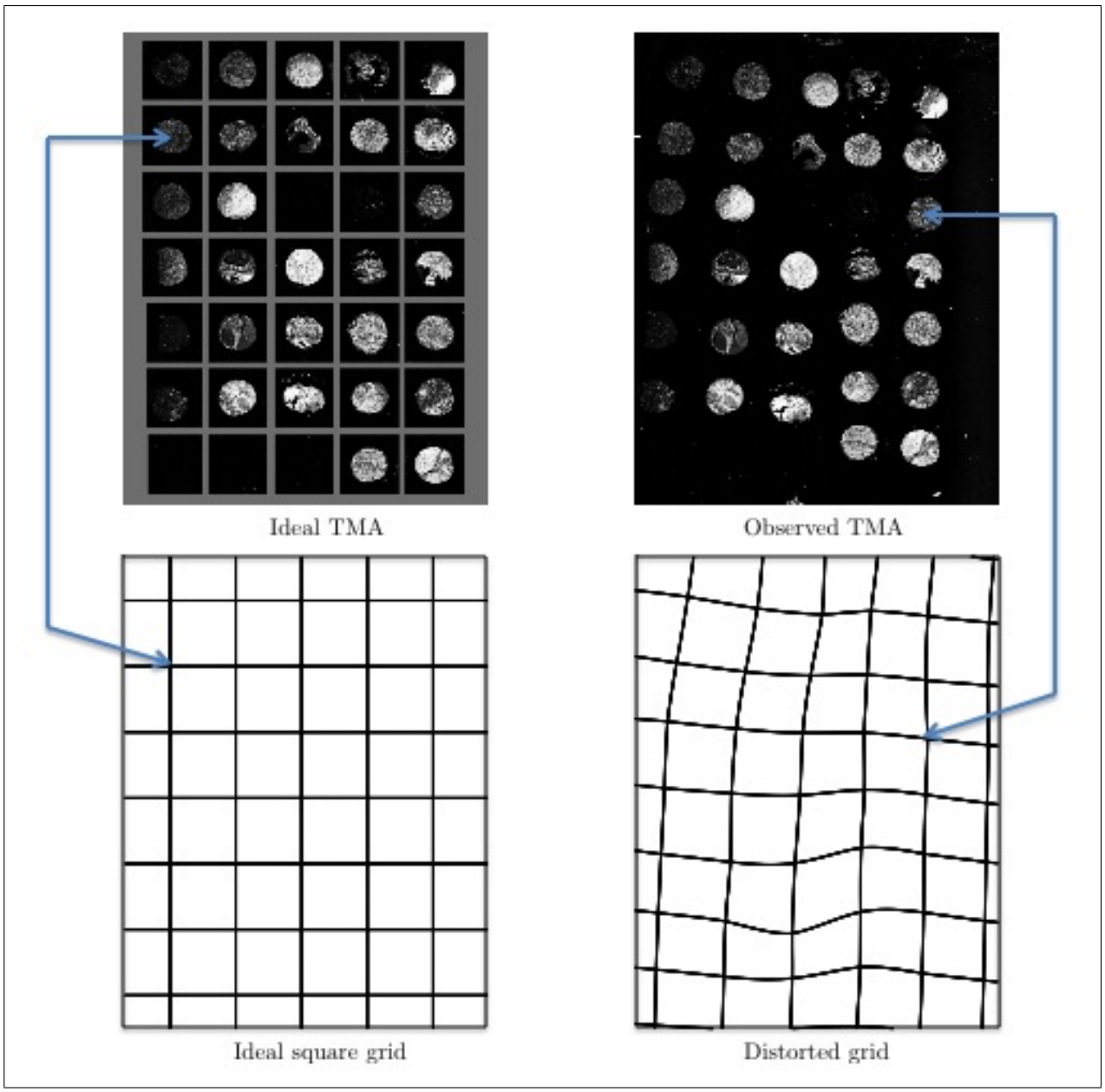

1.3 State-of-art of TMA de-arraying methods

Closely similar to TMAs, DNA microarrays (also known as bio-chips) are constructed by spotting DNA probes by robots with high precision according to a grid pattern. Numerous griding methods for microarrays were used to localize each DNA probes and find its row and column coordinates with

respect to the design grid. This procedure is called "de-arraying". Despite the similitude of these microarray concepts, existing "de-arraying" methods for microarrays are not adapted for TMAs because the grids are more highly deformed. Along with the commercialization of digital imaging devices for TMA analysis over the last decade, several methods for TMA "de-arraying" have been developed [17, 18, 19, 20, 21, 22]. In general terms, a "de-arraying" approach consists in two steps : (i) segmentation and localization of assembled tissue cores ; (ii) array coordinate (row and column coordinates) estimation of each core.

Firstly, for segmenting tissues, existing de-arraying methods usually assume that the histogram of a TMA image is bimodal. Under this assumption, these methods perform in general a thresholding by taking the local minimum between two highest peaks corresponding to the background and the foreground, of the image intensity histogram as global threshold. Various thresholding techniques were proposed from a simple thresholding as in [17] to more sophisticated methods such as the moment-preserving thresholding in [19], the automatic thresholding based on Savitsky-Golay filtered histogram in [20] or Otsu's method used in [21, 22]. To improve the segmentation result, pre-processing like contrast enhancement transform [22] or template matching [19] was applied. Morphological operators were also used as post-processing for removing outliers in the thresholded map as in [17, 22]. However, this underlying assumption is not satisfied in case of images acquired from novel fluorescence device because of their complex background. Due to the nature of fluorescence imaging, pixels corresponding to irrelevant objects – such as dusts, glue and washing stains – in the background have often high intensities resulting as a high peak in the intensity histogram ; in contrast, the intensities of pixels corresponding to tissue cores could be relatively lower. Hence, as a consequence, most of cores fail to be detected with a high threshold and there is a number of outliers corresponding to a low threshold value.

Secondly, for estimating row and column coordinates of each TMA cores, the methods mentioned above were generally based on distance and angle criteria to define the average spacing between the cores and the orientation of the observed grid. These criteria were derived simply from the distance between neighbor tissue cores [19], or from sophisticated measures such as the histogram of distance and angle [17] or the coefficients of the Hough transform [18] or even the Delaunay triangulation [22]. To deal with the case of missing tissue cores or the design of TMA grid in which some positions are left empty [16], linear or local bilinear interpolation were used as in [17, 22] for completing the grid. Whereas these methods yielded satisfactory results for further pathological analysis, they could not produce quantitative information about the deformation of the TMA grid which is an indicator for evaluating the quality of the manufactured input TMA. For that reason, we address this issue and develop a de-arraying mthod which is able to provide quantitative information about the deformation. Our approach allows management of traceability and quality control of the whole TMA manufacturing process.

1.4 Overview of the method

In this paper, we propose a fast and efficient approach for automated TMA de-arraying with the emphasis on fluorescence TMA images and modeling of TMA grid deformation. The proposed approach called ATMAD is based on the following image processing operations : core detection, core segmentation and estimation of the grid deformation. For the tissue localization step of the de-arraying procedure, we combine the detection and segmentation tasks to produce reliable inputs for the second step – the computation of the array coordinate of each tissue core. This second step is performed by using the deformation estimation module followed by a segmentation task to refine the result. The outline of our approach is shown in Fig. 2 which describes the two steps of the

FIGURE 2 – **Overview of our TMA de-arraying approach.** The proposed ATMAD approach consists in two steps : (i) tissue core localization ; (ii) estimation of array coordinates of tissue cores. The localization step is performed by combining a fast wavelet-based detection and an ellipse-shaped active contour to produce accurate core positions for the second step. The second step is dedicated to the estimation of the deformation of the TMA grid. The objective is to refine the de-arraying result by providing additionally potential positions of tissue cores which were not recognized at the first step. The de-arraying result is presented as a regular array to facilitate the seeking of row and column coordinates of each core.

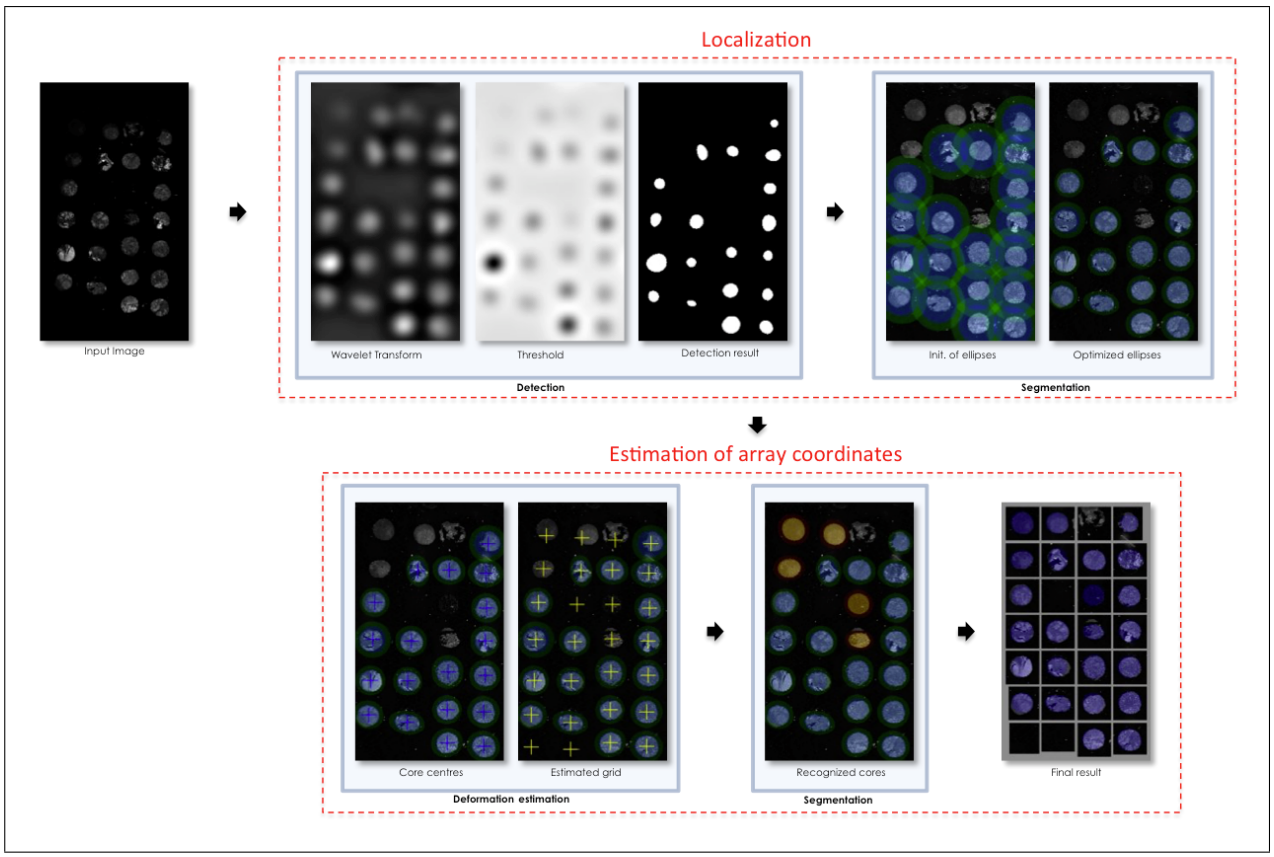

de-arraying procedure and the combination of the three image processing operations.

The "detection" operation (*i.e.* the detection) is based on a wavelet approach. In order to process images having large dynamic range, complex background and high noise level such as fluorescence images, we compute a stationary wavelet transform of the input TMA image at an appropriate scale to the tissue size – the average tissue core radius given by the manufacturer. By choosing the mother wavelet as a difference of Gaussians, we can deduce the closed-form expression of the wavelet atom at any desired scale and use it to perform directly the wavelet decomposition. Our technique is faster and more accurate than the well-known "à trous" algorithm [23]. The wavelet transform map is then locally thresholded to spatially adapt to the contrast between the foreground – corresponding to TMA cores – and the inhomogeneous background. The position of potential tissue cores is defined as the center of the connected components in the thresholded wavelet transform map.

To delineate the boundary of each tissue core and improve detection result, an ellipse-shaped

active contour [24] is used for segmenting the detected object at each position obtained from previous step. The segmented objects, which are too large or too small than the given average size of tissue sample or too elongated, will be considered as false detection and be discarded from the list of potential positions. This removal is essential to discard potential outliers and enhancing the reliability of the input for the estimation of row and column coordinates of TMA cores.

Instead of estimating directly the row and column coordinates of each core from the position list, we approximate the deformation of the TMA grid using the thin-plate model. In fact, the deformed grid is the image (in the sense of set theory) of the regular grid of design by the deformation. Given the deformation at some arbitrary points of the grid, the thin-plate interpolation allows to estimate it at other points [25]. The more we have known points, the more we estimate precisely the deformation. Once the deformation is approximated, the computation of row and column coordinates of each tissue core is therefore straightforward. By reformulating as an approximation problem and solving it iteratively, our method is robust to high non-linear deformations which were observed in most real TMA images. Moreover, according to the thin-plate model, the approximation yields information such as the average translation, the rotation angle, the bending energies along the horizontal and vertical axes, etc. These information are useful to assess the quality of the manufactured TMAs.

The remainder of this paper is organized as follows. In the next section, we describe the dearraying approach including a technical presentation of the "detection, "segmentation", "deformation estimation" tasks. We also figure out how the proposed approach is adapted for TMA images acquired with bright field microscopes. In Section "Results and discussion", we present the experimental results obtained from simulated and real data. Finally, the last section gathers the conclusions drawn from this research and details the future work.

2 Methodology

In our approach, the estimation of core positions on the input TMA image is subsequently refined in successive tasks by considering different image domains (*i.e.* patches or regions) in the input original image. Such a strategy allows not only to avoid unnecessary processing on non-content regions but also to reduce the acquisition time, storage and processing time of high resolution data. To distinguish the inputs and outputs of each task and facilitate the comprehension of the technical details, we present in Fig. 3 a diagram which illustrates a few notations which will be used throughout the paper.

2.1 TMA core Detection

The detection of approximately circular TMA cores can be performed by spot detection algorithms. Spot detection is a well-known topic in image processing (see [26] for a recent review). Over past decades, number of spot detection methods have been proposed [27, 28, 29, 30, 31]. To produce satisfactory results, most of these methods require fine adjustment of a critical parameter : the detection scale corresponding to the size of the objects of interest. Automatic selection of the detection scale is a challenging problem since the objects of interest may have different sizes or they may have the same size as the irrelevant objects in the background. Few methods of automatic scale selection [32, 33, 34] have been proposed recently. However, in the context of tissue microarrays, the diameter of assembled TMA cores is defined by the size of the needle used for extracting cores from paraffin tissue blocks. The determination of the scale parameter used for spot detection is straightforward from this measure which is often given by the manufacturer. We propose here a fast algorithm for tissue core detection by performing directly the wavelet decomposition

FIGURE 3 – **Illustration of core positions and notations.** The image u is defined on a rectangular domain Ω (shown in black rectangle). For each detected position $\mathbf{c}_n$ (red small dots), a patch P_n (red dashed squares) centered at $\mathbf{c}_n$ is extracted. The ellipse Γ_n (blue ellipses) with center $\mathbf{x}_{0,n}$ (blue crosses) is optimized to fit the object of interest which is located inside the patch P_n.

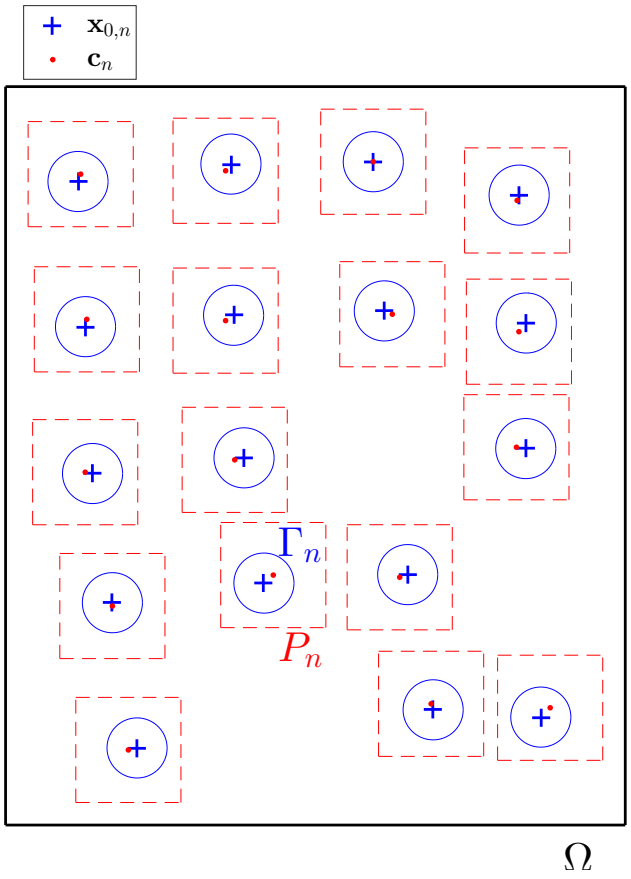

at the appropriate aforementioned scale and computing a locally-adaptive threshold of the wavelet coefficients.

2.1.1 Pre-processing

Wavelet-based detection techniques are known to be robust to non-stationary noises like Poisson noise or mixed-Poisson-Gaussian noise as in TMA images, acquired by bright field or fluorescence. Pre-processing operations such as image denoising or variance stabilization transform are thus not mandatory. However, our algorithm is primarily designed for detecting bright spots over a dark background, and especially adapted for fluorescence images. Bright field TMA images, in which the tissue cores are darker than the background, are first inverted before further processing.

2.1.2 Scale selection

Nowadays, standard TMAs are manufactured with a diameter of tissue core typically from 0.6 to 1.5 millimeters. Given an imaging resolution (pixel size), the optimal scale of wavelet decomposition

can be determined according to the core radius. If we denote r_{core} the expected average radius (in pixels) of TMA cores, the optimal scale index $\hat{j}$ of the wavelet decomposition that best fits the size of TMA cores is defined as :

$$\hat{j} = \underset{j \in \mathbb{N}^*}{\operatorname{argmin}} \left| r_{core} - 2^{j-1}\sigma_1 \right| \ , \tag{1}$$

where σ_1 is selected according to the pixel size.

2.1.3 Fast isotropic wavelet decomposition

In contrast to multiresolution approaches, our detection method requires only the wavelet decomposition at the appropriate selected scale. To compute the decomposition at a desired scale, usual wavelet transform techniques perform a sequence of successive convolutions which are used for computing iteratively the decomposition from the smallest scale to the coarsest scale. These techniques are time consuming when dealing with large images and high number of scales. Instead, to address to this computational issue, we build an dyadic isotropic wavelet frame $\{\psi_j\}_{j \geq 1}$ by choosing the scaling function ϕ_j as a Gaussian function whose variance v_j^2 is a function of scale $j \in \{1, \cdots, j_{\max}\}$ and $j_{\max}$ is the maximum index of the highest scale :

$$\phi_j(\mathbf{x}) = G_{v_j}(\mathbf{x}) = \frac{1}{2\pi v_j} \exp\left(-\frac{\|\mathbf{x}\|_2^2}{2v_j^2} \right), \tag{2}$$

where $\|\cdot\|_2$ denotes the Euclidean norm, $\mathbf{x} \in \Omega \subset \mathbb{R}^2$ is the pixel location in the rectangular domain Ω and

$$v_j^2 \ = \ \sum_{k=1}^{j} \sigma_k^2 \ = \ \sum_{k=1}^{j} 4^{k-1}\sigma_1^2 \ = \ \sigma_j^2 + v_{j-1}^2 \tag{3}$$

with $\sigma_k = 2^{k-1}\sigma_1$. Thanks to the semi-group property of Gaussian functions, the relationship between the scaling functions at subsequent scales can be expressed as :

$$\begin{aligned} \phi_j(\mathbf{x}) &= G_{\sqrt{\sigma_j^2 + v_{j-1}^2}}(\mathbf{x}) \\ &= G_{\sigma_j} \star G_{v_{j-1}}(\mathbf{x}) \ = \ G_{\sigma_j} \star \phi_{j-1}(\mathbf{x}), \end{aligned} \tag{4}$$

where $\star$ denotes the convolution operator. Therefore, the wavelet decomposition $\Psi_j u$ of $u : \Omega \subset \mathbb{R}^2 \to \mathbb{R}$ at the scale $j \in \{1, \cdots, j_{\max}\}$ is obtained by convolution of u with the wavelet atom ψ_j as :

$$\begin{aligned} \Psi_j u(\mathbf{x}) \ = \ \psi_j \star u(\mathbf{x}) &= (\phi_{j-1} - \phi_j) \star u(\mathbf{x}) \\ &= (G_{v_{j-1}} - G_{v_j}) \star u(\mathbf{x}), \end{aligned}$$

with the conventions $v_0^2 = 0$ and $G_0(\cdot) = \delta(\cdot)$ (Dirac delta function). For more technical details on the proposed wavelet frame and the wavelet decomposition and reconstruction algorithms, please refer to the Appendix section.

2.1.4 Locally-adaptive thresholding

While the wavelet decomposition plays the role of a filtering which reduces the noise and enhances the objects of interest, a common way to detect objects is to threshold the filtered image –

FIGURE 4 – **Wavelet atom and corresponding weighting function used for estimating the local distribution wavelet transform of a circular spot image.** From left to right : the image of a circular spot, its wavelet atom at the appropriate scale and its corresponding weighting function on the top row ; and their radial profile on the bottom row (red dashed lines delineate the radius of the spot).

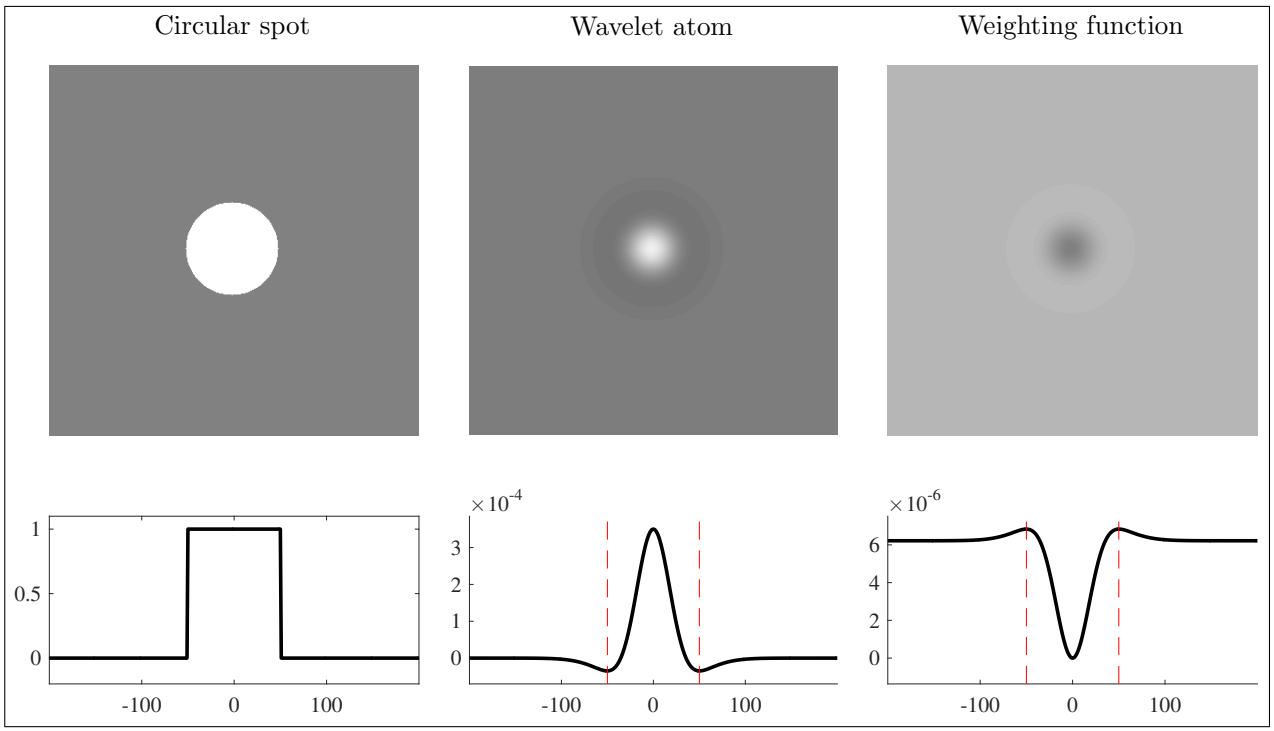

the wavelet decomposition of the input TMA image in our case. As depicted in [32], a global threshold is not appropriate to handle complex situations, especially when dealing with images acquired in fluorescence context because of their inhomogeneous background. To overcome this difficulty, we propose to define an adaptive threshold according to the local distribution of the wavelet decomposition $\Psi_{\hat{\jmath}} u$ previously computed. Accordingly, we consider the following statistical test at each point $\mathbf{x}$ of the TMA image u :

$$\begin{cases} \mathcal{H}_0 : & \mathbf{x} \text{ belongs to the background,} \\ \mathcal{H}_1 : & \mathbf{x} \text{ corresponds to tissue core (foreground).} \end{cases}$$

Pixels corresponding to tissue cores have strong positive responses in the wavelet decomposition. Under the null hypothesis $\mathcal{H}_0$, the wavelet coefficient $\Psi_{\hat{\jmath}} u(\mathbf{x})$, which follows the local distribution of the wavelet-decomposed-image background with mean $\mu(\mathbf{x})$ and variance $\nu^2(\mathbf{x})$, is lower than a certain value $\tau(\mathbf{x})$. Let $\mathbb{P}\left(\Psi_{\hat{\jmath}} u(\mathbf{x}) < \tau(\mathbf{x})\right)$ be the probability for a pixel $\mathbf{x}$ to be classified as "background" class. The threshold $\tau(\mathbf{x})$ is used to control the number of misclassification. Given a probability of false alarm $p_{\text{FA}} > 0$, the corresponding threshold τ_{FA} is selected such that the misclassification probability $\mathbb{P}\left(\Psi_{\hat{\jmath}} u(\mathbf{x}) \geq \tau_{\text{FA}}(\mathbf{x})\right)$ is lower than p_{FA}. By applying the conventional probabilistic Tchebychev's inequality, we get, $\forall \kappa(\mathbf{x}) > 0$:

$$\mathbb{P}\left(|\Psi_{\hat{\jmath}} u(\mathbf{x}) - \mu(\mathbf{x})| \geq \kappa(\mathbf{x})\right) \leq \frac{\nu^2(\mathbf{x})}{\kappa^2(\mathbf{x})}. \tag{5}$$

It follows that

$$\mathbb{P}\left(\Psi_{\hat{\jmath}}\, u(\mathbf{x}) \geq \mu(\mathbf{x}) + \kappa(\mathbf{x})\right) \leq \mathbb{P}\left(|\Psi_{\hat{\jmath}}\, u(\mathbf{x}) - \mu(\mathbf{x})| \geq \kappa(\mathbf{x})\right).$$

Now, let us define $\tau_{\text{FA}}(\mathbf{x}) = \mu(\mathbf{x}) + \kappa(\mathbf{x})$ and assume $(\nu^2(\mathbf{x})/\kappa^2(\mathbf{x})) \leq p_{\text{FA}}$ such that $\mathbb{P}\left(\Psi_{\hat{\jmath}}\, u(\mathbf{x}) \geq \tau_{\text{FA}}(\mathbf{x})\right) \leq p_{\text{FA}}$. Finally,

$$\tau_{\text{FA}}(\mathbf{x}) \geq \mu(\mathbf{x}) + \frac{\nu(\mathbf{x})}{\sqrt{p_{\text{FA}}}} \tag{6}$$

and the adaptive threshold $\tau_{\text{FA}}(\mathbf{x})$ is controlled by the p-value p_{FA} set by the user.

To determine the threshold $\tau_{\text{FA}}(\mathbf{x})$, the local mean $\mu(\mathbf{x})$ and the local variance $\nu^2(\mathbf{x})$ of the image background on the wavelet decomposition $\Psi_{\hat{\jmath}}\, u$ are required. However, prior knowledge about the image background distribution is unfortunately not available in most cases. We consider thus empirical estimations of μ and ν^2 at each point $\mathbf{x}$ from $\Psi_{\hat{\jmath}}\, u$:

$$\hat{\mu}(\mathbf{x}) = g \star \Psi_{\hat{\jmath}}\, u(\mathbf{x}), \tag{7}$$

$$\hat{\nu}^2(\mathbf{x}) = g \star (\Psi_{\hat{\jmath}}\, u)^2(\mathbf{x}) - \hat{\mu}^2(\mathbf{x}), \tag{8}$$

where $g(\cdot)$ is a weighting positive function (i.e. $\|g(\cdot)\|_1 = 1$, $\|\cdot\|_1$ is the L_1 norm and $g(\mathbf{x}) \geq 0, \forall \mathbf{x} \in \Omega$) mainly used to avoid the estimation of the background distribution statistics being biased from coefficients corresponding to the foreground. By construction, $\hat{\mu}(\mathbf{x})$ and $\hat{\nu}^2(\mathbf{x})$ are weighted estimators derived from $\Psi_{\hat{\jmath}}\, u$ which is a filtered version of u by the band-pass filter $\psi_{\hat{\jmath}}$ in order to enhance the objects of radius r_{core}. It is thus convenient to define the weighting function g according to the wavelet atom $\psi_{\hat{\jmath}}$. By using an affine transform which implies the positivity and the normalization conditions, we propose a candidate for $g(\cdot)$ as following :

$$\hat{g}(\mathbf{x}) = \frac{-\psi_{\hat{\jmath}}(\mathbf{x}) + \sup \psi_{\hat{\jmath}}}{\|-\psi_{\hat{\jmath}} + \sup \psi_{\hat{\jmath}}\|_1}, \tag{9}$$

where $\sup \psi_{\hat{\jmath}} = \|\psi_{\hat{\jmath}}\|_\infty$ denotes the supremum (L_∞ norm) of $\psi_{\hat{\jmath}}$ and $\|-\psi_{\hat{\jmath}} + \sup \psi_{\hat{\jmath}}\|_1$ is the normalization factor to ensure $\|\hat{g}(\cdot)\|_1 = 1$. The choice of this candidate is clarified in Fig. 4 showing the wavelet atom and its derived weighting function according to a given circular spot. The proposed weighting which is constructed from the wavelet atom has the same size of the considered spot and has a hollow shape at the center (see right column in Fig. 4). This specific shape allows to reduce the impact of high wavelet coefficients corresponding to foreground pixels on the estimation of the background statistics.

By substituting the empirical estimators to $\mu(\mathbf{x})$ and $\nu^2(\mathbf{x})$, we obtain the estimated detection threshold :

$$\hat{\tau}_{\text{FA}}(\mathbf{x}) = \hat{\mu}(\mathbf{x}) + \frac{\hat{\nu}(\mathbf{x})}{\sqrt{p_{\text{FA}}}}. \tag{10}$$

Thresholding the wavelet decomposition $\Psi_{\hat{\jmath}}\, u$ with respect to $\hat{\tau}_{\text{FA}}$ results in a binary image $I_{\text{FA}} : \Omega \to \{0, 1\}$:

$$I_{\text{FA}}(\mathbf{x}) = \begin{cases} 1 & \text{if } \Psi_{\hat{\jmath}}\, u(\mathbf{x}) \geq \tau_{\text{FA}}(\mathbf{x}) \\ 0 & \text{otherwise} \end{cases} \tag{11}$$

where each connected component in I_{FA} represents a region which is potentially a tissue core of the TMA image. The gravity centers of these regions (or detection position) will be used as inputs for estimating the array coordinates of TMA cores. However, the detection reliability has a great impact on the de-arraying outcome : few false detections may lead to severely inaccurate results.

Removing false detections (i.e. outliers) is then crucial. To this end, the size of detected regions seems to be a relevant criterion since the core size is given in most cases by the TMA manufacturer. Although, due to the complexity of backgrounds, it may be highly different from the true core size. Instead of exploiting the imprecise information derived from the binary detection map I_{FA}, we perform an active-contour-based segmentation to delineate the objects at each detected position. Also, we re-use the segmentation results to confirm and improve the preliminary detection results.

2.2 Segmentation of TMA cores

As depicted in previous section, the detection binary image I_{FA} does not allow us to accurately determine the size of detected objects. Active contours [35] are typically well appropriate in our context since they can evolve to closely delineate the object borders and thus yield an estimation of the TMA core size. The family of parametric active contours presented below will help to refine the detected position and the size of TMA cores and eventually to determine the orientation of the potential core if it was deformed during the manufacturing process.

Since the seminal paper of Kass, Witkin, and Terzopoulos, active contour models (or snakes) [35] have been successfully used to detect discontinuities, detect objects of interest or segment images, especially in bioimaging [36]). General purpose closed contours are generally controlled by elastic forces based on local curvature and image based potentials [35, 37, 38, 39]. The curve evolves from its initial starting position towards the target object. The optimization of the underlying energy functional is traditionally performed using variational principles and finite differences techniques, which needs an appropriate initialization to converge to a relevant solution. At the end of the nineties and beginning of the 2000's, geodesic active contours [40] based on the theory of surfaces evolution and geometric flows have been introduced to segment an arbitrary number of highly complex objects in the image. In our TMA context, the 2D shapes of tissue cores can be actually well estimated by ellipse-shaped active contours which belong to the family of parametric deformable templates.

Application-tailored parametrized templates introduced by Yuille *et al.* [41] were proposed in cases where strong a priori knowledge about the shape being analyzed is available (e.g. eyes or lips in human faces [41]). The models are hand-built using simple parametrized 2D geometric representations. Another line of research focused on models of random deformations for a given initial shape (deformable template). Grenander *et al.* [42, 43] obtained the first promising results in image segmentation by considering statistical deformable models which describe the statistics of local deformations applied to an original template. Markov models and Monte-Carlo techniques have been introduced in this context to derive optimal random deformations estimates from image data [42, 43, 44, 45, 46]. In the approach initially proposed by Cootes *et al.* [47] and successfully applied to object tracking [45], the shape structure and the parameters describing its deformations are learned from a training set of representative shapes. Meanwhile, Staib and Duncan [48] proposed to combine parametric snakes (B-splines) to the standard decomposition on a Fourier basis to analyze deformable biomedical structures. All these methods are generally robust to noise but computationally demanding if stochastic iterative procedures are used to conduct the minimization and no initial guess close to the optimal solution is provided. Very recently "snakescules" [49] combined to fast algorithms and Markov point process [50] have been proposed along the same philosophy but dedicated to the detection of cells or nuclei in fluorescence microscopy images.

Finally, the ellipse fitting concept has been furthemore introduced by Thévenaz *et al.* as an extension of the simple circle-shaped active contour [49] which can be defined just by two points [24]. As a consequence, a triplet of points is necessary to parametrize the ellipse-shaped version. However, this parametrization which has an extra degree of freedom increases the complexity of

FIGURE 5 – **Pair of concentric and coaxial ellipses.** The outer ellipse Γ (red curve) has an area twice larger than the inner ellipse Γ' (blue curve). These ellipses determine two domains of the same area : an elliptical outer ring (shown in light gray) and an elliptical inner core (dark gray).

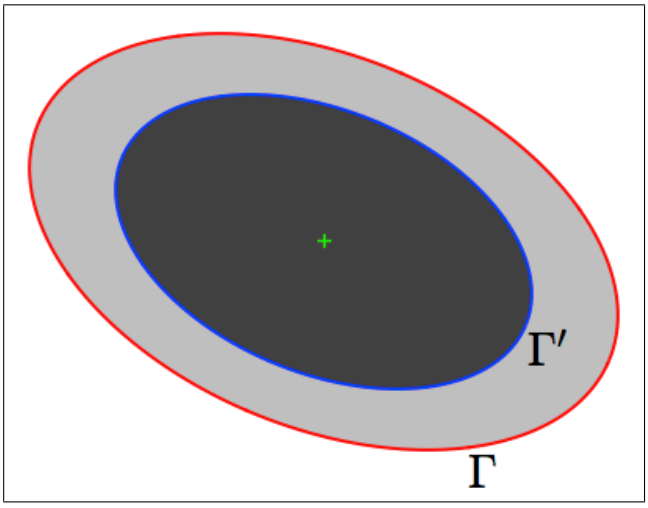

the model and makes the optimization of ellipse parameters more challenging when compared to the circle-shaped model. To overcome these difficulties, an alternative way was proposed in [51] : the ellipses are configured by their center, their axes and the angle between their major axis and the horizontal. Under this configuration, the cost function defined as the contrast between the core and the ring defined by the pair of ellipses (see Fig. 5) – and the derivatives with respect to the ellipse parameters could be calculated efficiently by using the Green's theorem [48]. Nevertheless, the Green's theorem cannot be applied with no error in the discrete setting and digitized images. In order to handle properly the ellipse parametrization described in [51] instead of [24] in the discrete setting, we propose a pixel-based smooth approximation of the underlying cost energy functional. Our approximation allows us to calculate properly the derivatives of the cost function with respect to the ellipse parameters and is not based on the Green's theorem also used in [48] for energy minimization.

2.2.1 Definition of the ellipse-based energy

More formally, let Γ be the outer ellipse with parameters $\{\mathbf{x}_0, a, b, \theta\}$ where $\mathbf{x}_0 = (x_0, y_0)$ is the center, a and b are the semi major and minor axes respectively, and θ is the angle of rotation. The inner ellipse Γ' is defined as a concentric and coaxial ellipse of Γ such the latter has an area (denoted $|\Gamma|$) twice larger than the former : $|\Gamma| = 2|\Gamma'|$ (see Fig. 5). The factor 2 ensures that the area of the elliptical outer ring is equal to the area of the elliptical inner core. Let us consider a rectangular image patch P containing a potential TMA core associated to a connected component estimated by the detection method in the early stage. The ellipse energy (or cost function) is defined as a normalized image contrast between the two domains $\Gamma' \subset \Gamma \subset P$ where P is a rectangular domain

in the image domain Ω which contains a single TMA core [52, 24] :

$$J(u,\Gamma) = \frac{1}{ab}\left(\int_{\Gamma\setminus\Gamma'} u(\mathbf{x})\ d\mathbf{x} - \int_{\Gamma'} u(\mathbf{x})\ d\mathbf{x}\right) \tag{12}$$
$$= \frac{1}{ab}\left(\int_{\Gamma} u(\mathbf{x})\ d\mathbf{x} - 2\int_{\Gamma'} u(\mathbf{x})\ d\mathbf{x}\right).$$

To handle discrete images, the continuous image u defined in (12) can be replaced by its sampled version as follows :

$$J(u,\Gamma) = \frac{1}{ab}\sum_{\mathbf{x}\in P\cap\mathbb{Z}^2} (\mathbb{1}_{\Gamma}[\mathbf{x}] - 2\ \mathbb{1}_{\Gamma'}[\mathbf{x}])\, u[\mathbf{x}] \tag{13}$$

where $u[\mathbf{x}]$ is the discrete sample of $u(\mathbf{x})$ and $\mathbb{1}[\cdot]$ denotes the set indicator function such as $\mathbb{1}_{\Gamma}[\mathbf{x}] = 1$ if $\mathbf{x} \in \Gamma$ and 0 otherwise. However, there are two major drawbacks while considering this energy function. Firstly, the calculation of the energy gradient is not trivial in the discrete setting since the indicator functions in (13) are piecewise constant which are not differentiable at some points. Secondly, due to sampling effect, brutal switch of the membership of some points from a domain to another may happen just with an infinitesimal change in the ellipse parameters, giving rise to severe numerical instabilities. Smooth approximations of the underlying piecewise constant functions is recommended to overcome both discontinuity and sampling problems. The calculations of partial derivatives of the energy functional is facilitated if we can define a fuzzy membership to avoid abrupt domain switches (see Fig. 8a and 8b). Our goal is then to build an approximation which favors the computation of the partial derivative of the energy with respect to each ellipse parameter as much as possible. First, we consider the following quadratic form :

$$\|\mathbf{x}\|_{\Gamma}^2 = \left\| \begin{bmatrix} a^{-1} & 0 \\ 0 & b^{-1} \end{bmatrix} \begin{bmatrix} \cos\theta & \sin\theta \\ -\sin\theta & \cos\theta \end{bmatrix} \mathbf{x} \right\|_2^2. \tag{14}$$

For a given point $\mathbf{x}$, $\|\mathbf{x}-\mathbf{x}_0\|_{\Gamma}$ is a normalized metric between $\mathbf{x}$ and the ellipse center $\mathbf{x}_0$ induced by the geometry of the ellipse Γ. A pixel $\mathbf{x}$ belongs to the interior of the ellipse Γ if and only if $\|\mathbf{x}-\mathbf{x}_0\|_{\Gamma}^2 \leq 1$ since $\|\mathbf{x}-\mathbf{x}_0\|_{\Gamma}^2$ is always positive. The term $\mathbb{1}_{\Gamma}[\mathbf{x}]$ can be then expressed by a function of $\|\mathbf{x}-\mathbf{x}_0\|_{\Gamma}$ as $\mathbb{1}_{\Gamma}[\mathbf{x}] = \mathbb{1}_{]-\infty,1]}[\|\mathbf{x}-\mathbf{x}_0\|_{\Gamma}^2]$. Moreover, we need to find a smooth function which closely approximates $\mathbb{1}_{]-\infty,1]}$ as investigated in [38, 24] and has simple derivative. We realized that the graph of $\mathbb{1}_{]-\infty,1]}$ looks similar to the C^{∞} S-shaped logistic curve whose the derivative is easy to compute. Let us consider therefore the following logistic function :

$$S_{\epsilon}(t) = \frac{1}{1+e^{\frac{t-1}{\epsilon}}} \underset{\epsilon\to 0}{\longrightarrow} \mathbb{1}_{]-\infty,1]}(t), \tag{15}$$

where $\epsilon > 0$ controls the steepness of the curve (see the plot of $t \longmapsto S_{\epsilon}(t)$ in Fig. 6 for several values of ϵ). The smaller ϵ, the closer the curve S_{ϵ} approaches the graph of the indicator function $\mathbb{1}_{]-\infty,1]}$. Thanks to the property of logistic functions, the derivative of S_{ϵ} can be easily computed as $S'_{\epsilon}(t) = -\epsilon^{-1}S_{\epsilon}(t)\,(1-S_{\epsilon}(t))$. Finally, the energy functional has the following form [24] :

$$J(u,\Gamma) = \frac{1}{ab}\sum_{\mathbf{x}\in P\cap\mathbb{Z}^2} w_{\epsilon}(\|\mathbf{x}-\mathbf{x}_0\|_{\Gamma}^2)\, u[\mathbf{x}]\ , \tag{16}$$

with $w_{\epsilon}(t) = S_{\epsilon}(t) - 2S_{\epsilon}(2t) = \dfrac{1}{1+e^{\frac{t-1}{\epsilon}}} - \dfrac{2}{1+e^{\frac{2t-1}{\epsilon}}}$. For illustration, we present in Fig. 7 the plot of w_{ϵ} whose the term $w_{\epsilon}(\|\mathbf{x}-\mathbf{x}_0\|_{\Gamma}^2)$ is nothing else than a smooth approximation of the piecewise constant function $\mathbf{x}_0 \longmapsto \mathbb{1}_{\Gamma}[\mathbf{x}] - 2\ \mathbb{1}_{\Gamma'}[\mathbf{x}]$. These weights are very similar to those described in [38] and based on the arctan function.

FIGURE 6 – **Approximation of the indicator function by logistic curves.** The smaller ϵ, the closer the S-shaped curve S_ϵ approaches the graph of $\mathbb{1}_{]-\infty,1]}$.

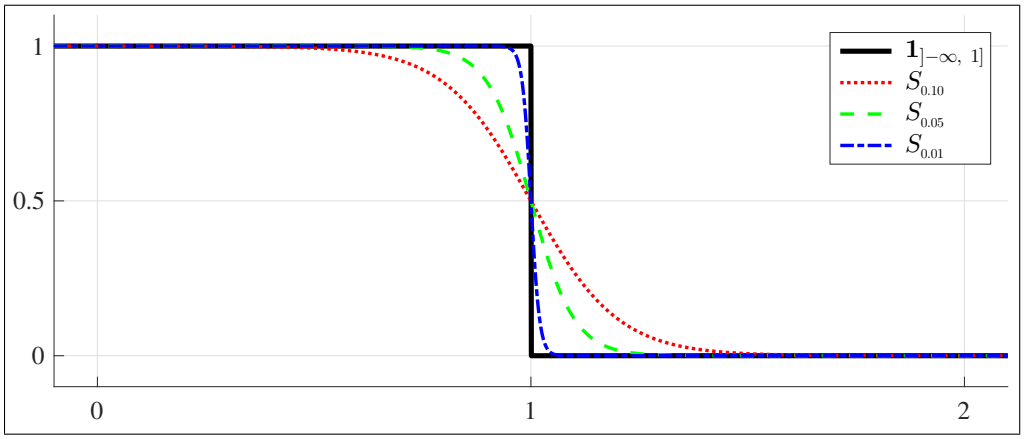

2.2.2 Calculation of partial derivatives

By applying the derivation rules of composite functions, the partial derivatives of the energy with respect to each ellipse parameter $\{\mathbf{x}_0, a, b, \theta\}$ are given by :

$$\begin{cases} \frac{\partial J(u,\Gamma)}{\partial x_0} = \frac{1}{ab}\sum_{\mathbf{x}} u[\mathbf{x}] w'_\epsilon\left(\|\mathbf{x}-\mathbf{x}_0\|^2_\Gamma\right) \frac{\partial \|\mathbf{x}-\mathbf{x}_0\|^2_\Gamma}{\partial x_0}, \\ \frac{\partial J(u,\Gamma)}{\partial y_0} = \frac{1}{ab}\sum_{\mathbf{x}} u[\mathbf{x}] w'_\epsilon\left(\|\mathbf{x}-\mathbf{x}_0\|^2_\Gamma\right) \frac{\partial \|\mathbf{x}-\mathbf{x}_0\|^2_\Gamma}{\partial y_0}, \\ \frac{\partial J(u,\Gamma)}{\partial \theta} = \frac{1}{ab}\sum_{\mathbf{x}} u[\mathbf{x}] w'_\epsilon\left(\|\mathbf{x}-\mathbf{x}_0\|^2_\Gamma\right) \frac{\partial \|\mathbf{x}-\mathbf{x}_0\|^2_\Gamma}{\partial \theta}, \\ \frac{\partial J(u,\Gamma)}{\partial a} = \frac{1}{ab}\sum_{\mathbf{x}} u[\mathbf{x}] w'_\epsilon\left(\|\mathbf{x}-\mathbf{x}_0\|^2_\Gamma\right) \frac{\partial \|\mathbf{x}-\mathbf{x}_0\|^2_\Gamma}{\partial a} - \frac{J(u,\Gamma)}{a}, \\ \frac{\partial J(u,\Gamma)}{\partial b} = \frac{1}{ab}\sum_{\mathbf{x}} u[\mathbf{x}] w'_\epsilon\left(\|\mathbf{x}-\mathbf{x}_0\|^2_\Gamma\right) \frac{\partial \|\mathbf{x}-\mathbf{x}_0\|^2_\Gamma}{\partial b} - \frac{J(u,\Gamma)}{b}, \end{cases}$$

$$\text{where } w'_\epsilon(t) = \frac{4S_\epsilon(2t)\left(1-S_\epsilon(2t)\right) - S_\epsilon(t)\left(1-S_\epsilon(t)\right)}{\epsilon}$$

$$= \frac{1}{\epsilon}\left[\frac{4e^{\frac{2t-1}{\epsilon}}}{\left(1+e^{\frac{2t-1}{\epsilon}}\right)^2} - \frac{e^{\frac{t-1}{\epsilon}}}{\left(1+e^{\frac{t-1}{\epsilon}}\right)^2}\right]$$

and the calculation of partial derivatives of $\|\mathbf{x}-\mathbf{x}_0\|^2_\Gamma$ are detailed in the Appendix. As depicted in Fig. 8c, for a given parametrization $\{\mathbf{x}_0, a, b, \theta\}$, the term $w'_\epsilon\left(\|\mathbf{x}-\mathbf{x}_0\|^2_\Gamma\right)$ vanishes for most of points $\mathbf{x}$. Thus, the computation of the partial derivatives $J(u,\Gamma)$ takes account only few points near the ellipse boundaries where $w'_\epsilon\left(\|.-\mathbf{x}_0\|^2_\Gamma\right)$ is non-zero. Our smooth approximation which is adapted for discrete images produces similar expressions of the partial derivatives of the ellipse energy when comparing with those described in [51] for continuous images. It can be viewed as the expression of the Green's theorem in the discrete setting and an alternative to the optimization presented in [44].

2.2.3 Multi-ellipse segmentation for multi-tissue core analysis

Let $\{\mathbf{c}_n\}_{1\leq n\leq N}$ be the centroids of the connected components of the binary detection map I_{FA}. In the original image u, we extract a rectangular patch P_n centered at $\mathbf{c}_n$ with a radius ρ larger

FIGURE 7 – **The weights w_ϵ.** $w_\epsilon\left(\|\mathbf{x}-\mathbf{x}_0\|^2_\Gamma\right)$ approximates $\mathbb{1}_\Gamma[\mathbf{x}]-2\,\mathbb{1}_{\Gamma'}[\mathbf{x}]$ whose the normalized radial profile is presented by the graph of the piecewise constant function $t \longmapsto \mathbb{1}_{]-\infty,\ 1]}(t) - 2\,\mathbb{1}_{]-\infty,\ 0.5]}(t)$.

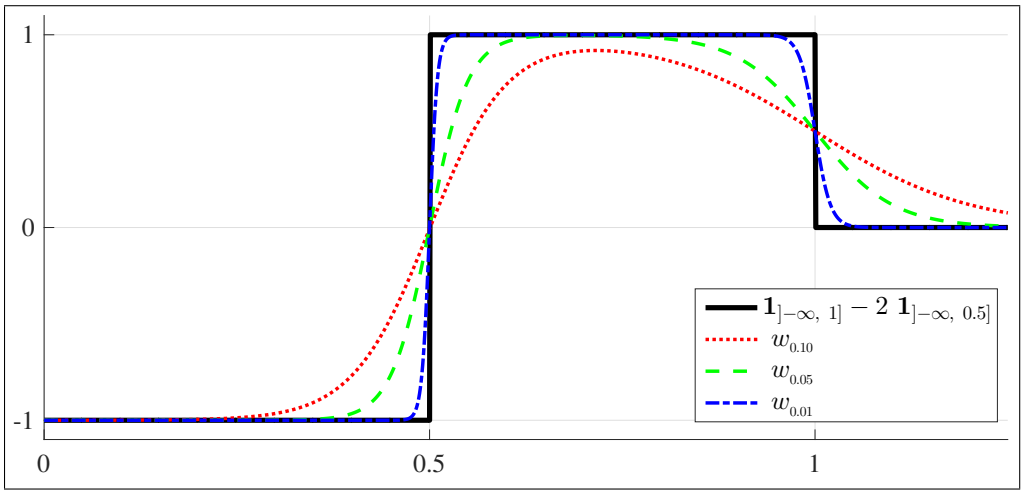

than the given tissue core radius r_{core} (for example, $\rho = 2r_{core}$). Let us define

$$\Pi_{\rho,\mathbf{c}_n} u = \{u[\mathbf{x}],\ \|\mathbf{x}-\mathbf{c}_n\|_\infty \leq \rho\}\,, \tag{17}$$

where $\mathbf{x} = (x, y) \in P_n$, $\|\mathbf{x}\|_\infty = \sup(|x|, |y|)$ and $\Pi_{\rho,\mathbf{c}_n}\cdot$ denotes the patch extraction operator with center $\mathbf{c}_n$ and radius ρ. In order to perform a multi-object segmentation, we consider the following multi-ellipse optimization problem :

$$\begin{aligned} &\underset{\Gamma_1,\ldots,\Gamma_N}{\arg\min} \sum_{n=1}^{N}\left\{\frac{1}{a_n b_n}\sum_{\mathbf{x}} w_\epsilon\Big(\|\mathbf{x}-\mathbf{x}_0^n\|^2_{\Gamma_n}\Big)\Pi_{\rho,\mathbf{c}_n}u[\mathbf{x}]\right\} \\ &\text{subject to } (\Gamma_1,\Gamma_2,\ldots,\Gamma_N)\in\Upsilon\ , \end{aligned} \tag{18}$$

where $\{\mathbf{x}_{0,n}, a_n, b_n, \theta_n\}$ are the parameters of the ellipse Γ_n and Υ is a set of constraints to ensure the ellipses fall into an acceptable range of configurations. In practice, we typically set

$$\begin{aligned} \Upsilon = \{\ &\left\|\mathbf{x}_{0,n}-\mathbf{x}_{0,n'}\right\|_2 > \rho; \\ &\|\mathbf{x}_{0,n}-\mathbf{c}_n\|_\infty \leq \rho_{\max}; \\ &r_{\min}\leq a_n, b_n \leq r_{\max}; \\ &\theta_{\min}\leq\theta_n\leq\theta_{\max} \qquad \}_{1\leq n,n'\leq N}\ , \end{aligned}$$

for some predefined values $\rho_{\max}, r_{\min}, r_{\max}, \theta_{\min}, \theta_{\max}$ set according to the extracted patch positions and the allowed sizes and orientations of tissue cores. The constraint $\left\|\mathbf{x}_{0,n}-\mathbf{x}_{0,n'}\right\|_2 > \rho$ which prevents the distance between two ellipse centers being too close helps to avoid the overlapping of segmented tissue cores. In what follows, we denote $\mathcal{J}(u,\Gamma_1,\cdots,\Gamma_n)$ the global cost function associated with the optimization problem (18).

By construction, the function $\mathcal{J}(u,\Gamma_1,\cdots,\Gamma_n)$ is differentiable with respect to $(\Gamma_1,\ldots,\Gamma_N)$. The common way to minimize $\mathcal{J}(u,\Gamma_1,\cdots,\Gamma_n)$ under the constraint set Υ is to use a gradient method

FIGURE 8 – **Inner and outer domain membership under discrete setting.** Points in the inner core are marked by dark gray squares and those in the outer ring are marked by lighter gray squares. From left to right : (a) abrupt domain switch for points in the neighbor of ellipse boundaries (red and blue curves) ; (b) fuzzy membership with transition zones (marked by purple squares) ; and (c) first order derivative of the function w_ϵ (zero values are shown in gray).

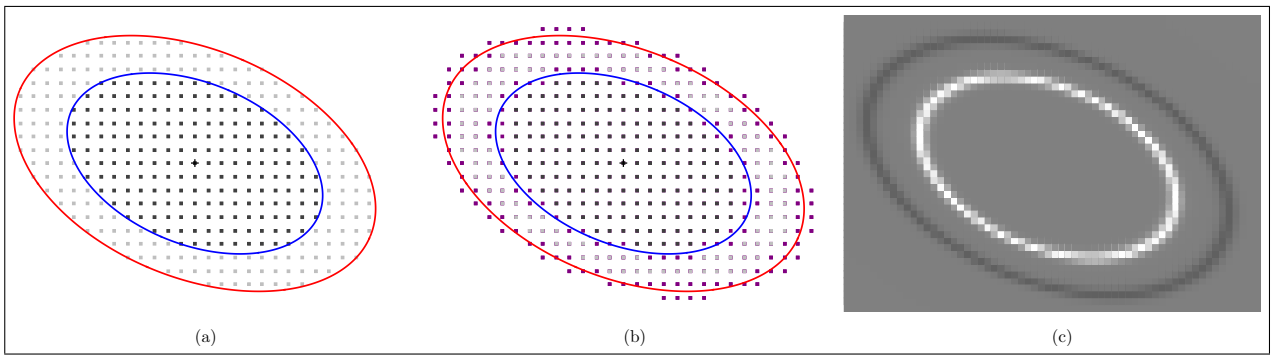

whose performance depends on how efficient is the computation of the gradient of $\mathcal{J}(u, \Gamma_1, \cdots, \Gamma_n)$. Since $\mathcal{J}(u, \Gamma_1, \cdots, \Gamma_n)$ is a linear combination of separable functions, therefore, the gradient can be simply obtained as :

$$\nabla\mathcal{J}(u, \Gamma_1, \cdots, \Gamma_n) = \begin{pmatrix} \nabla J(\Pi_{\rho,\mathbf{c}_1} u, \Gamma_1) \\ \vdots \\ \nabla J(\Pi_{\rho,\mathbf{c}_N} u, \Gamma_N) \end{pmatrix}, \tag{19}$$

where

$$J(\Pi_{\rho,\mathbf{c}_n} u, \Gamma_n) = \frac{1}{a_n b_n} \sum_{\mathbf{x}\in\Gamma_n} w_\epsilon \left(\|\mathbf{x} - \mathbf{x}_0^n\|^2_{\Gamma_n} \right) \Pi_{\rho,\mathbf{c}_n} u[\mathbf{x}]$$

and the expressions of its partial derivatives are given in (17).

The result of the multi-ellipse optimization problem (18) is a set of ellipses $\{\Gamma_n\}_{1\leq n\leq N}$ which manages to fit the objects located in the regions of interest $\{\Pi_{\rho,\mathbf{c}_n} u\}_{1\leq n\leq N}$. Furthermore, given the major axes of these ellipses and the TMA core radius r_{core}, we discard the tiny, giant and flattened ellipses and we keep those which are most similar to the expected tissue cores. The center of the selected ellipse allows us to determine the position of the recognized TMA core. This reference position will be used to determine the array coordinates of the corresponding tissue core. In the following, we denote $\mathcal{X}_0 = \{\mathbf{x}_{0,n}\}_{n\in\{1,\ldots,N\}}$ as the set of centers of the N reliable and selected ellipses.

2.3 Estimation of array coordinate and TMA core positions

An ideal TMA is the one which has tissue cores perfectly aligned in both horizontal and vertical directions and equally spaced according to a regular square grid. The array coordinate $\mathbf{p} = (k, l) \in \mathbb{Z}^2$ of a core can be simply obtained by drawing two orthogonal lines crossed at the considered core position. However, due to the deformation of the design TMA grid, the lines passing through tissue cores and their nearest neighbors may be slightly inclined with respect to the horizontal or vertical axes. Moreover, the direction of these lines may have a large spectrum of variations which makes more challenging the tracking of tissue cores over a given direction. To deal with this deformation, existing TMA de-arraying methods use usually distance-and-angle-based criteria for the purpose of

FIGURE 9 – **Affine approximation of the grid deformation.** The distorted grid Λ which one only observe partially the set of point $\mathcal{X}_0 \subset \Lambda$ (shown in blue crosses) is approximated by the oblique (regular) grid Λ_0 (black circled dots). The latter is characterized by the average distance $\bar{d}$ between its points, two principal directions which are presented by two vectors $(\mathbf{e_1}, \mathbf{e_2})$ (red arrows), and the global translation $\hat{\mathbf{t}}$ (green arrow) of the grid with respect to the origin $(0, 0)$ (gray square dot).

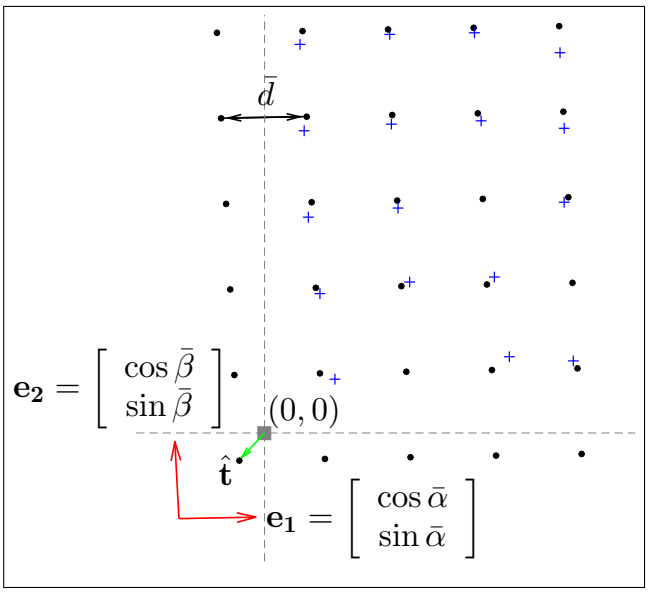

defining the neighborhood of TMA cores. Although this approach is robust to estimate the average core-to-core distance and the two principal directions of the deformed core grid, it may fail for some well-detected cores whose the position is strongly distorted with respect to their neighbors. In order to avoid this failure, we introduce an algorithm for estimating iteratively the deformation of the TMA grid in a way that the grid which is warped by the estimated deformation at an iteration gets closer to the observed TMA grid. To this end, we assume that the deformation of the TMA grid can be decomposed by linear and non-linear parts. Under this assumption, we estimate the linear part of the deformation by defining an oblique grid (affine warping) which is derived from the detected core positions as the initialization of the warped grid (see Fig. 9). The latter is used to find nearby cores that will be taken into account to compute an estimator of the grid deformation by using the thin-plate interpolation [25] if we do an analogy with material deformation.

2.3.1 Estimation of the linear deformation

Our goal is to approximate the distorted TMA grid Λ (which is observed partially with the set of point $\mathcal{X}_0$) by an oblique grid Λ_0 which minimizes the distance between them in the way that the deformation of the grid is approximated by a 2D affine transform. For this purpose, we consider the set $\mathcal{C}_0$ of core pairs whose each pair $(\mathbf{x}_{0,n}, \mathbf{x}_{0,n'})$ is formed by an element of $\mathcal{X}_0$ and one of its four nearest neighbors with respect to the Euclidean distance

$$\mathcal{C}_0 = \left\{ (\mathbf{x}_{0,n}, \mathbf{x}_{0,n'}) \in \mathcal{X}_0 \times \mathcal{X}_0,\ \mathbf{x}_{0,n'} \in \mathcal{N}(\mathbf{x}_{0,n}) \right\},$$

where $\mathcal{N}(\mathbf{x}_{0,n})$ denotes the 4-neighborhood of $\mathbf{x}_{0,n}$. To estimate the average core-to-core distance $\bar{d}_{cc}$, we compute the trimmed mean (denoted TM) of the length of the segment defined by the pair

$(\mathbf{x}_{0,n}, \mathbf{x}_{0,n'})$ of $\mathcal{C}_0$ by discarding the most extreme values (typically 30%) :

$$\bar{d} = \mathrm{TM}_{30\%} \left\{ \|\mathbf{x}_{0,n} - \mathbf{x}_{0,n'}\|_2 \right\}_{(\mathbf{x}_{0,n}, \mathbf{x}_{0,n'}) \in \mathcal{C}_0} \ . \tag{20}$$

Let $\mathrm{ang}(\mathbf{x}_{0,n}, \mathbf{x}_{0,n'})$ be the angle between the line passing through $(\mathbf{x}_{0,n}, \mathbf{x}_{0,n'})$ and the horizontal axis such that $-0.25\pi \leq \mathrm{ang}(\mathbf{x}_{0,n}, \mathbf{x}_{0,n'}) \leq 0.75\pi$. By analogy, we define the two principal angles of the deformed TMA grid as follows :

$$\bar{\alpha} = \mathrm{TM}_{30\%} \left\{ \mathrm{ang}(\mathbf{x}_{0,n}, \mathbf{x}_{0,n'}) \leq \frac{\pi}{4} \right\},$$
$$\bar{\beta} = \mathrm{TM}_{30\%} \left\{ \mathrm{ang}(\mathbf{x}_{0,n}, \mathbf{x}_{0,n'}) \geq \frac{\pi}{4} \right\}.$$

Finally, we denote $\hat{\mathbf{t}}$ as the global translation of the distorted TMA grid with respect to the origin that best minimizes the distance between the set $\mathcal{X}_0$ and the linearly-estimated grid Λ_0

$$\hat{\mathbf{t}} = \arg\min_{\mathbf{t}} \sum_{n=1}^{N} \min_{\mathbf{p} \in \mathbb{Z}^2} \|\mathbf{t} + \mathcal{F}(\mathbf{p}) - \mathbf{x}_{0,n}\|_2^2 \tag{21}$$

where $\mathcal{F}$ maps each array coordinates $\mathbf{p} \in \mathbb{Z}^2$ to a position of Λ_0 corrected by $\hat{\mathbf{t}}$ and

$$\mathcal{F}(\mathbf{p}) = \bar{d} \underbrace{\begin{bmatrix} \cos\bar{\alpha} & \cos\bar{\beta} \\ \sin\bar{\alpha} & \sin\bar{\beta} \end{bmatrix}}_{\mathbf{M}_{\bar{\alpha},\bar{\beta}}} \mathbf{p} \ . \tag{22}$$

Note that $\mathbf{M}_{\bar{\alpha},\bar{\beta}}$ is a change-of-basis matrix of unit column vectors and $\bar{d}$ is a scaling factor which transforms array coordinates (elements of $\mathbb{Z}^2$) to real spatial positions (in $\Omega \subset \mathbb{R}^2$). The resulting oblique grid is parametrized with four parameters $\{\bar{d}, \bar{\alpha}, \bar{\beta}, \hat{t}\}$ and represents the affine part of the grid deformation. We thus arrive at the affine mapping function : $\mathcal{A}(\mathbf{p}) = \hat{\mathbf{t}} + \mathcal{F}(\mathbf{p}) \in \Lambda_0$. The oblique grid Λ_0 will serve as initialization to estimate of the non-linear deformation of the grid. Figure 9 illustrates an example showing the oblique grid obtained from a given set of points as well as its estimated parameters.

2.3.2 Thin-plate-based estimation of the deformation

Let $\Lambda^\star$ be the ideal design TMA grid with $(0, 0)$ as origin and d the ideal distance between two neighboring cores along the horizontal and vertical axes. The mapping is then defined as :

$$\mathbf{y}^\star_{\mathbf{p}} = d\mathbf{p} \in \Lambda^\star, \forall \mathbf{p} \in \mathbb{Z}^2.$$

The deformation $\mathcal{D}$ maps each point $\mathbf{y}^\star_{\mathbf{p}} \in \Lambda^\star$ onto a point $\mathbf{y}_{\mathbf{p}} = \mathcal{D}(\mathbf{y}^\star_{\mathbf{p}})$ in the distorted grid Λ. In order to estimate the deformation $\mathcal{D}$ at all points of the grid $\Lambda^\star$, we aim at approximating this set from the observed set $\mathcal{X}_0 = \{\mathbf{x}_{0,n}\}$ by using the thin-plate splines as an interpolant. Indeed, given a set of points $\mathcal{D}^{-1}\mathcal{X}_0 = \left\{\mathcal{D}^{-1}(\mathbf{x}_{0,n})\right\}_{n \in \{1,\ldots,N\}}$, the coefficients of the interpolating thin-plate splines are the minimizers of a quadratic function which is the first approximation of the bending energy of the mapping from $\mathcal{D}^{-1}\mathcal{X}_0$ to the set of target points $\mathcal{X}_0$ (see [25]). Nevertheless, unlike the usual framework [25], the correspondence between the two sets of points is not established, that is $\mathcal{D}^{-1}\mathcal{X}_0$ is unknown. Instead of investigating a matching method to determine $\mathcal{D}^{-1}\mathcal{X}_0$, we propose to build

FIGURE 10 – **Correspondence between the ideal grid and the observed distorted grid.** At an iteration m, the estimated deformation $\mathcal{D}^{(m)}$ maps each point $\mathbf{y}_{\mathbf{p}}^{\star}$ of the ideal square grid $\Lambda^{\star}$ (shown in square dots on the left) onto a point $\mathbf{y}_{\mathbf{p}}^{(m)} = \mathcal{D}^{(m)}(\mathbf{y}_{\mathbf{p}}^{(m)})$ in the warped grid $\Lambda^{(m)}$ (circled dots on the right) which manages to fit the observed set of points $\mathcal{X}_0$ (blue crosses). A position $\mathbf{x}_{0,n} \in \mathcal{X}_0$ is associated to a position $\mathbf{y}_{\mathbf{p}}^{\star}$ if $\mathbf{x}_{0,n}$ is located within a radius δ from $\mathbf{y}_{\mathbf{p}}^{(m)}$ (blue dotted circles). Associated positions are marked in red.

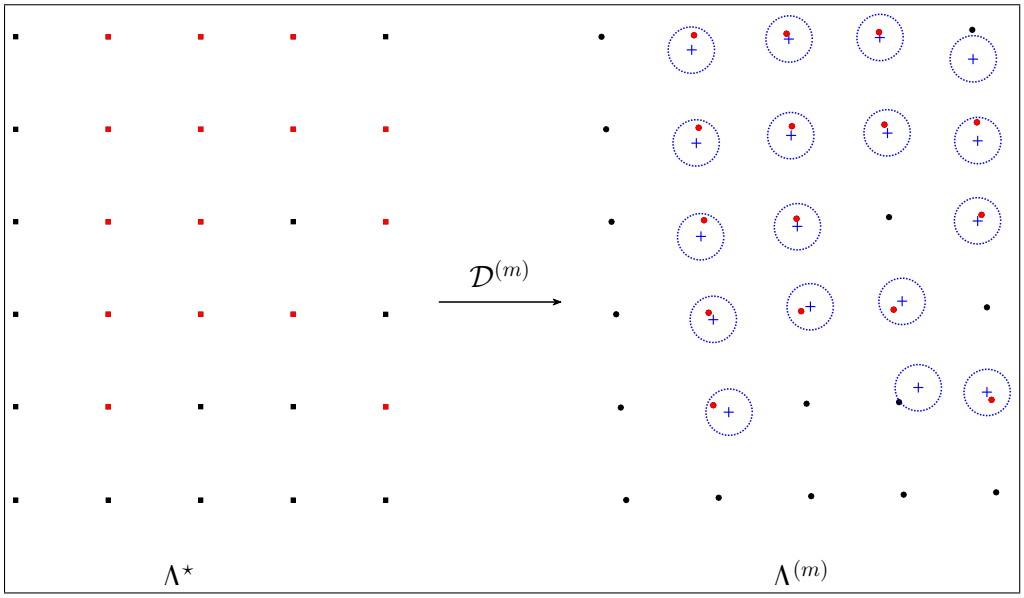

a sequence of grids $\{\Lambda^{(m)}\}_{m\geq 0}$ which evolves iteratively to fit $\mathcal{X}_0$. We initialize this sequence with the oblique grid $\Lambda^{(0)} = \Lambda_0$ previously computed. The linear approximation of $\mathcal{D}$ is then as follows :

$$\begin{aligned} \mathbf{y}_{\mathbf{p}}^{(0)} &= \mathcal{D}^{(0)}(\mathbf{y}_{\mathbf{p}}^{\star}) \\ &= \hat{\mathbf{t}} + \frac{\bar{d}}{d}\begin{bmatrix} \cos\bar{\alpha} & \cos\bar{\beta} \\ \sin\bar{\alpha} & \sin\bar{\beta} \end{bmatrix}\mathbf{p}. \end{aligned} \tag{23}$$

At iteration m, a core position $\mathbf{x}_{0,n} \in \mathcal{X}_0$ is associated to a position $\mathbf{y}_{\mathbf{p}}^{\star}$ if the former is located within a radius δ from $\mathbf{y}_{\mathbf{p}}^{(m)} = \mathcal{D}^{(m)}(\mathbf{y}_{\mathbf{p}}^{\star})$. Pairs of associated positions establish therefore the correspondence between the ideal grid $\Lambda^{\star}$ and the set of observed point $\mathcal{X}_0$. We also note that all the positions of $\Lambda^{\star}$ do not have a corresponding position in $\mathcal{X}_0$ as shown in Fig. 10 mainly because the cardinal of sets are not the same. Let $\mathcal{P}^{(m)}$ be the set of pairs of associated positions :

$$\mathcal{P}^{(m)} = \left\{ \left(\mathbf{x}_{0,n}, \mathbf{y}_{\mathbf{p}}^{\star}\right),\ \|\mathcal{D}^{(m)}(\mathbf{y}_{\mathbf{p}}^{\star}) - \mathbf{x}_{0,n}\|_2 \leq \delta \right\}. \tag{24}$$

Assume that $N^{(m)}$ is the number of elements of $\mathcal{P}^{(m)}$. The objective is to estimate the deformation $\mathcal{D}^{(m)}$ from the set of $N^{(m)}$ associated pairs $(\mathbf{x}_{0,n}, \mathbf{y}_{\mathbf{p}}^{\star})$. According to [25], we define the Gram's matrix $\left\{\mathbf{K}_{n,n'}^{(m)}\right\}_{1\leq n,n'\leq N^{(m)}}$ as follows :

$$\mathbf{K}_{n,n'}^{(m)} = \left\|\mathbf{x}_{0,n} - \mathbf{x}_{0,n'}\right\|_2^2 \log \left\|\mathbf{x}_{0,n} - \mathbf{x}_{0,n'}\right\|_2^2, \tag{25}$$

and the additional matrices as :

$$\mathbf{Y}^{(m)} = \begin{bmatrix} 1 & 1 & \dots & 1 \\ \mathbf{y}_{\mathbf{p}_1} & \mathbf{y}_{\mathbf{p}_2} & \cdots & \mathbf{y}_{\mathbf{p}_{N^{(m)}}} \end{bmatrix}, \tag{26}$$

$$\mathbf{L}^{(m)} = \left[\begin{array}{c|c} \mathbf{K}^{(m)} & \mathbf{Y}^{(m)} \\ \hline \mathbf{Y}^{(m)\top} & 0 \end{array}\right], \tag{27}$$

$$\mathbf{X}^{(m)} = \begin{bmatrix} \mathbf{x}_{0,1} & \mathbf{x}_{0,2} & \dots & \mathbf{x}_{0,N^{(m)}} & 0 & 0 & 0 \end{bmatrix}, \tag{28}$$

$$\mathbf{W}^{(m)} = \left(\left(\mathbf{L}^{(m)} \right)^{-1} \left(\mathbf{X}^{(m)} \right)^{\top} \right)^{\top}, \tag{29}$$

and $\mathbf{W}^{(m)} = (\mathbf{w}_1^{(m)}, \mathbf{w}_2^{(m)}, \dots, \mathbf{w}_{N^{(m)}}^{(m)})^{\top}$. By using the entries of the matrix $\mathbf{W}^{(m)}$, the estimators of the deformation $\mathcal{D}$ and of the grid Λ at the next iteration $m+1$ are therefore defined as :

$$\begin{aligned} \mathbf{y}_{\mathbf{p}}^{(m+1)} = {} & \mathbf{w}_{N^{(m)}+1}^{(m)} + \left[\mathbf{w}_{N^{(m)}+2}^{(m)} \mathbf{w}_{N^{(m)}+3}^{(m)} \right] \mathbf{y}_{\mathbf{p}}^{\star} \\ & + \sum_{n=1}^{N^{(m)}} \mathbf{w}_n^{(m)} (\|\mathbf{x}_{0,n} - \mathbf{y}_{\mathbf{p}}^{\star}\|_2^2 \log \|\mathbf{x}_{0,n} - \mathbf{y}_{\mathbf{p}}^{\star}\|_2^2) \ . \end{aligned} \tag{30}$$

This iterative scheme will be stopped at the iteration $m^* = m$ if there are no change between $\Lambda^{(m)}$ and $\Lambda^{(m+1)}$. At convergence, the row and column coordinates of a detected cores of position $\mathbf{x}_{0,n} \in \mathcal{X}_0$ is simply given by :

$$\hat{\mathbf{p}} = \underset{\mathbf{p} \in \mathbb{Z}^2}{\arg\min} \|\mathbf{x}_{0,n} - \mathcal{D}^{(m^*)}(\mathbf{y}_{\mathbf{p}}^{\star})\|_2^2 \ . \tag{31}$$

Moreover, since the grid $\Lambda^{(m^*)}$ is an estimator of the deformed TMA grid Λ which is partially observed in $\mathcal{X}_0$, it can be used as approximated positions to recognize tissue cores which are missed during detection and segmentation processes. Indeed, to refine de-arraying result, we perform another multi-ellipse optimization at the position of remaining nodes of the grid $\Lambda^{(m^*)}$. If there are ellipses that meet the size and the roundness criteria of standard cores, we add them to the list of detected core position and adjust the coefficients of the thin-plate splines according to the new list. An example of TMA de-arraying is depicted in Fig. 14 showing the gain of our method in term of tissue core detection.

3 Results and discussion

Description of data sets

To evaluate our de-arraying ATMAD approach, we selected a number of DNA microarray and tissue microarray images including those which are artificially simulated and those which are acquired in both bright field and fluorescence modes. The selected images were collected from various sources and can be classified into three data sets.

The first set is a collection of binary images generated by Dr Yinhai Wang in [22] as pseudo TMA slides. This data set was artificially created by taking account of different possible situations occurring during the TMA manufacturing process, including rotations and stretches of the design grid as well as irregularities in the size and the shape of tissue cores. The average core radius is approximately $r_{core} = 15$ pixels for all images. The whole set of all these simulated images and ground truths can be freely downloaded at `https://get.google.com/albumarchive/117531880452844036890`.

FIGURE 11 – **Example of de-arraying on simulated images.** From left to right : TMAs with the grid deformation varying from low to high. From top to bottom : original images, de-arraying result by the proposed method with segmentation module deactivated/activated, ground truth given by Dr Jinhai Wang. The obtained de-arraying results are presented in array form with recognized spot positions marked by green boxes.

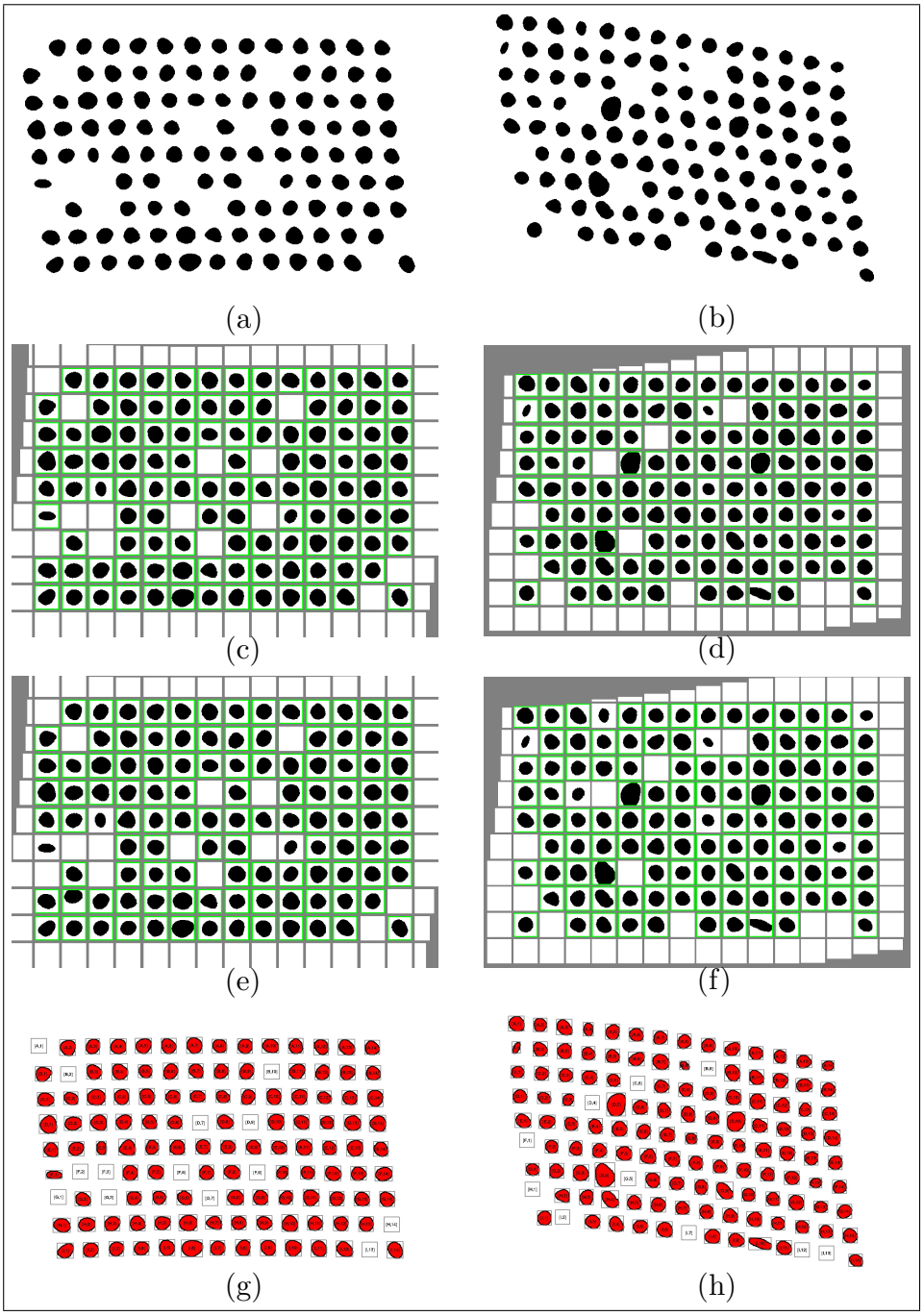

The second data set is composed of color TMA images from the AIDS and Cancer Specimen Resource (ACSR) Digital Library of the University of California San Francisco (`http://acsr.ucsf.edu`). This online library – managed and visualized by Aperio's WebScope software – contains several hundreds of tissue specimens which are mostly stained with H&E (Hematoxylin and Eosin) stain and are imaged by bright field microscopy technique. For this experiment, we considered down-sampled version (with the magnification between 0.4X and 0.6X) of the original images hosted on ACSR's server in order to reduce the processing time. The considered resolutions correspond to images of approximately 1000×1000 pixels, on which the TMA cores have radius of only a few dozen pixels but it is sufficient for our approach to localize them.

The third set for the evaluation includes fluorescence high-dynamic-range (HDR) images showing DNA microarray and tissue microarray slides. Provided by the courtesy of Innopsys company, these HDR images which were saved in 16-bit-TIFF format were acquired using a scanner called InnoScan 1100AL (see `https://www.innopsys.com/en/lifesciences-products/microarrays/innoscan/innoscan-1100-` for more details). The latter which is equipped with three excitation lasers (488 nm, 532 nm and 625 nm compatible with cyanine dyes such as Cy2, Cy3 and Cy5 respectively). It can perform simultaneously the acquisition on each excitation channel and provides up to three color fluorescence images. The maximal scan area supported by the mentioned device is $22\ mm \times 74\ mm$ corresponding to the size of typical microscopy slides used in most biological laboratories nowadays. For the same reason with ACSR's images, we selected typical images acquired by this Innopsys's scanner with spatial resolutions varying in a range from 10 to 40 μm per pixel in this experiment instead of using those with higher resolution (up to $0.5\mu m$ per pixel or a 20X magnification equivalently). Indeed, considering such images of low resolution and small size as input data not only enables efficient and low-memory-requirement processing but also requires very short scanning time – less than just five minutes with a resolution of 10 μm per pixel when compared with typically several hours of acquisition at sub-micrometer resolutions.

Regarding the complexity of the data sets, it contains difficult cases such as irregular and non-rounded shapes, fragmented cores as well as low contrasts between image background and foreground. Sophisticated array design with incomplete (missing cores) rows and columns is also present in the image set for the purpose of testing the robustness of our de-arraying approach (see Fig. 11-14).

3.1 Experimental results and algorithm evaluation

For the first and second data sets which contain images with dark spots and bright background, we performed first an color inversion before further processing. The de-arraying procedure was directly applied on binary and grayscale images. Multi-channel color images as in the case of ACSR's data require a conversion to grayscale such as a simple average over all channels which we used in these experiments.

In order to evaluate the performance of our ATMAD algorithm, we analyzed the obtained results by considering two criteria : (i) the rate of samples which are successfully recognized and (ii) the rate of samples whose array coordinates are correctly estimated. For this purpose, the de-arraying ATMAD outcome was compared with the ground-truth provided for simulated data or with manual annotation in the case of real data. Moreover, intermediary results of the de-arraying procedure were also investigated to allow a step-by-step evaluation. Finally, we computed the bending energies along the horizontal and vertical direction of the estimated grid deformation from the thin plate splines coefficients to quantify the deformation level and asset the quality of the estimation.

FIGURE 12 – **Example of de-arraying on bright field TMA image.** (a) Original image : H&E stained TMA on ACSR's database with ID 550-T0011-01. (b) Manual annotation used for comparison with de-arraying results. (c)-(d) De-arraying results obtained with the deactivation/activation of the segmentation module. These results and the manual annotation are represented in array format with recognized cores marked by green boxes.

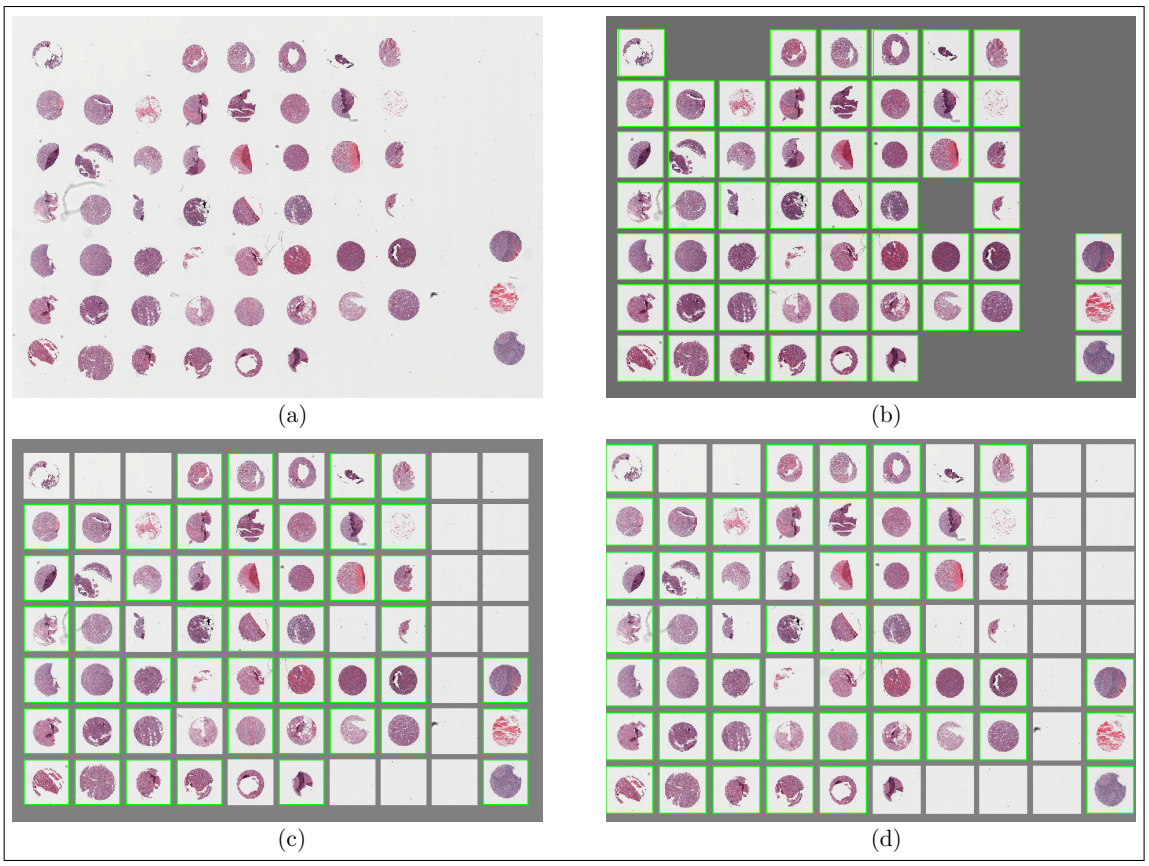

3.2 Simulated images

We evaluated ATMAD on the Wang's data set. We evaluated the results in the two cases of deactivation and activation of the segmentation algorithm in the de-arraying procedure (see Fig. 2). If the segmentation algorithm is not activated, the spot localization is performed only with the detection algorithm. The removal of unreliable cores based on the size and shape criteria is then disabled. The full procedure is evaluated in the second case and the detection and the segmentation algorithm jointly localize the potential spots, which reduces false detections.

De-arraying simulated images with different levels of deformation is illustrated in Fig. 11. The top row shows the original images. The two middle rows show the de-arraying outcomes obtained with deactivation and activation of the segmentation algorithm respectively. The recognized spot positions are marked by green boxes and correctly aligned in a array to facilitate localization and identification. The bottom row of Fig. 11 shows the ground-truth provided by the data set expert.

As expected, in this case when the background is constant, our algorithm provided an accuracy of 100% in overall even though the localization of spots is done only by the fast wavelet-based detection

FIGURE 13 – **Example of de-arraying on a fluorescence DNA microarray image.** (a) Contrast-enhanced original image. (b) De-arraying result of the proposed method presented in array format. (c) Manual annotations in array format. For comparison purpose, recognized DNA spots are marked by green boxes.

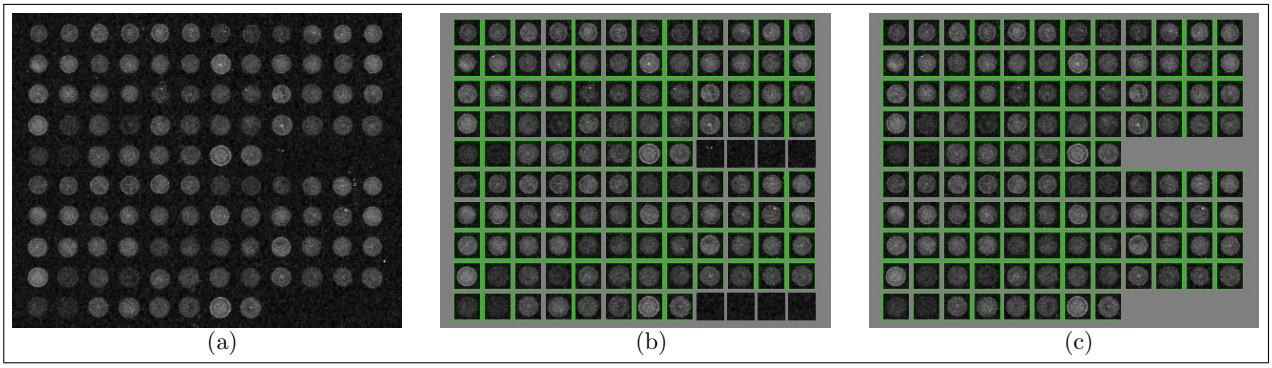

(a) (b) (c)

algorithm. On the second row of Fig. 11 showing the de-arraying obtained on three examples when the segmentation module were deactivated, we can see that all spots were successfully recognized and their array coordinates were correctly estimated. This result is identical to those reported by Wang *et al.* in [22]. The de-arraying obtained with the segmentation module activated is closely similar (see the three bottom rows of Fig. 11) but its overall accuracy score is only 98.1% – slightly lower if the segmentarion algorithm is not used. This inferior score is a direct consequence of the fact that all existing spots were not recognized by the spot localizer due to segmentation failure or elimination. Despite a smaller number of correct spot positions, the estimation of the array coordinate yielded exact results for successfully recognized spots comparing with the ground-truth. In terms of deformation estimation, the estimated potential spot positions provided by the de-arraying under two settings are almost identical. It thus allows us to localize spots which were not recognized and demonstrates the robustness of our method for estimating the grid deformation.

3.3 Bright field images

We have noticed that in the previous experiments with simulated data, our wavelet-based detection method was able to localize all spots on images with constant background. In the case of bright field TMA images whose background is not constant but generally homogeneous, this approach might still be efficient for spot localization since the situation is much more simpler than in fluorescence imaging. The evaluation of the proposed algorithm on ACRS's image set with the segmentation module deactivated/activated was therefore performed to investigate the performance if the segmentation algorithm is used or not.

In Fig. 12, the de-arraying on a H&E stained TMA image containing irregularities in the shape of tissue cores is illustrated. The original input image shown in Fig. 12a is the slide cut #9 of the TMA whose the ID is 550-T0011-01 on ACSR's database. The de-arraying results obtained with the deactivation and the activation of the segmentation module are depicted in Fig. 12c and 12d respectively. To evaluate the accuracy of these results, we consider in Fig. 12b a reference de-arraying obtained by manual annotation. The latter is presented in the same format (*i.e.* an array representation) as those of the automated de-arraying outcomes to facilitate comparison.

Comparing with an accuracy of 100% obtained on simulated data, localization only based the

wavelet method achieved barely 90.12% of existing TMA cores on ACSR's data. Indeed, it failed generally to recognize cores with inner hole or cores which are split into parts (see Fig. 12c) since the shape of these cores implies that the wavelet coefficients at their position are lower than the detection threshold – resulting to non detection. Activating the segmentation module does not improve successful recognition rate of the localization step due to the use of detected core position for initializing the ellipse fitting. In our interest, the main role of this module in the localization step is to measure the size and the roundness of detected objects in order to eliminate false detection and to provide reliable input for the estimation of the grid deformation. For this reason, only 86.53% of existing cores were correctly recognized during the localization step with the combination of the detection and the segmentation modules due to the segmentation failure and the elimination of outliers. In spite of the difference between the localization results obtained with the deactivation/activation of the segmentation module, the estimation of the grid deformation using these results however yielded similar de-arraying outcomes as illustrated in Fig. 12c and 12d. The overall accuracy of the de-arraying procedure with the segmentation module deactivated is 90.12% compared to 89.27% with the same module activated. Under the latter setting, the final recognition rate of tissue cores has increased by 2.74% with respect to the rate obtained after the localization phase. This improvement is due to the segmentation performed using the potential position which is provided by the estimation of the grid deformation to recognize missed cores during the first phase of the de-arraying procedure (for example, some fragmented cores or cores with inner hole were additionally recognized as shown in Fig. 12d in comparison with Fig. 12c). This approach is quite useful when the number of undetected cores by using our wavelet-based method is important specially in the case of fluorescence images on which the contrast between the background and the foreground is often significantly weaker than on bright field images.

3.4 Fluorescence images

In contrast with experiments on simulated and bright field images, the performance of our de-arraying algorithm was evaluated on more challenging Innopsys's image set by considering the activation of the segmentation algorithm. The deactivation of this module was not considered in this experiment since the non-homogeneity of the image background may lead to false positives during the wavelet-based detection process and possibly to severe errors of the de-arraying result if these false detection are not removed. The combination of the detection and the segmentation module in the localization phase as described in Section 'Methodology' can handle this undesired situation by providing not only the potential position of existing DNA or TMA samples but also the size and the ratio between the major axis and the minor axis of the object found at each detected position to eliminate false detection.

Figures 13 and 14 show the de-arraying results obtained on two fluorescence images – a DNA microarray and a tissue microarray. For the illustrated DNA microarray, we presented in Fig. 11 only the original image, the final de-arraying result and the corresponding manual annotations. Whereas, intermediate results were additionally illustrated in Fig. 12 besides the original image as well as the final result and the ground truth in the case of TMA image to allow step-by-step evaluation.

As expected, the proposed ATMAD algorithm achieved 100% accuracy in overall on DNA microarray images (see Fig. 13b and 13c). This perfect score was obtained due to the regularity of the size, the shape and the grid of spotted DNA samples which facilitates the localization and the estimation of the array coordinates of each spot. It is however not possible to reach such an accuracy on TMA images because of the deformation of TMA grid and the irregularities of TMA cores. As a consequence, only 64.38% of existing cores were correctly recognized by our wavelet-based detection.

FIGURE 14 – **Example of de-arraying on fluorescence TMA image.** (a) Contrast-enhanced original image. (b) Detection map (accurate detection is marked in white, wrong detection is marked in red). (c) Segmentation of TMA cores (recognized cores are colored by blue ellipses). (d) Estimated TMA grid (potential core position is marked by a red cross). (e) Recognized TMA cores (cores which are additionally recognized are colored by orange ellipses). (f) Final de-arraying result in array format (recognized core position is marked by green box). (g) Manual annotations for comparison.

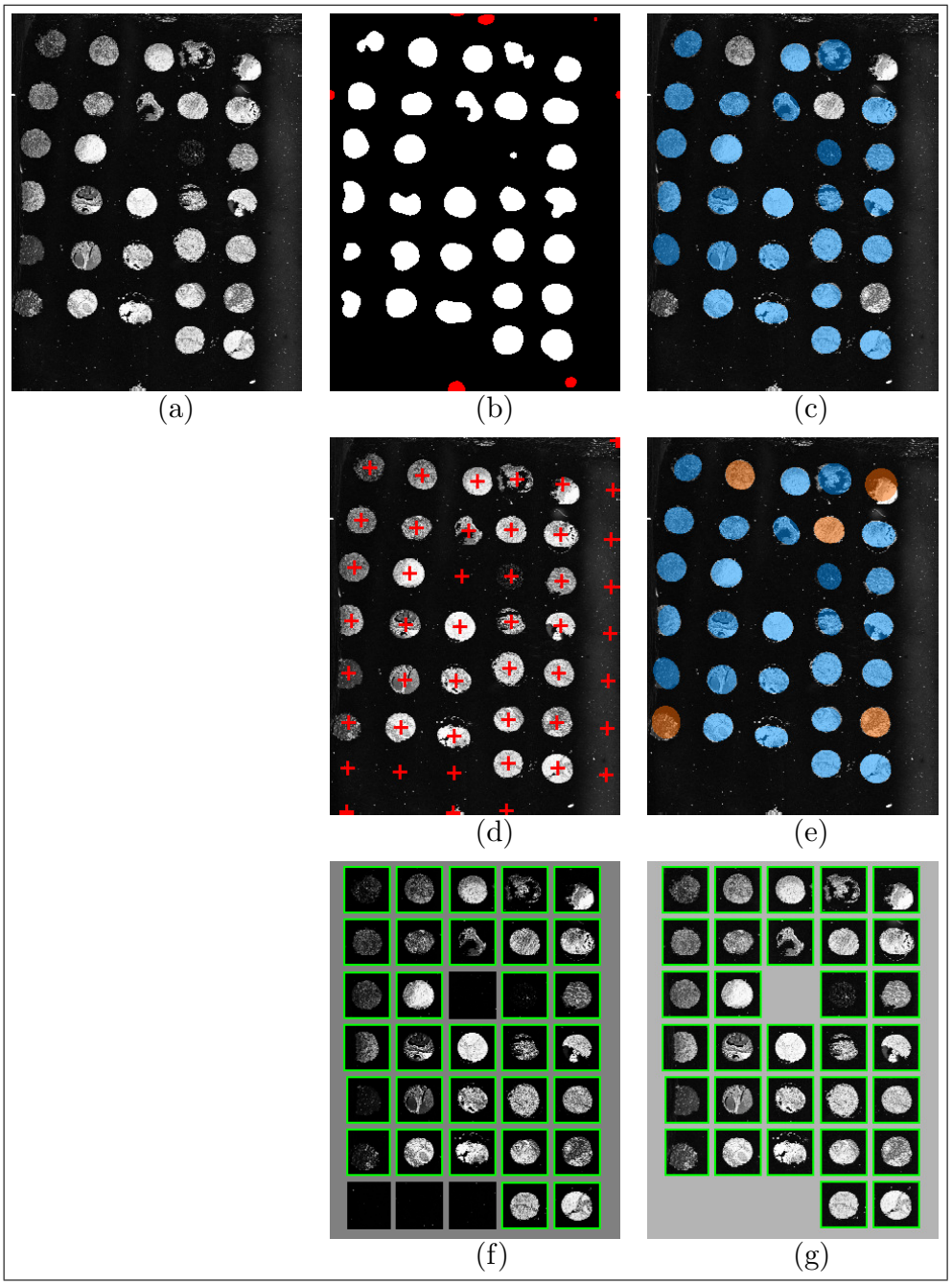

False detection mostly accurred on images with complex background such as those illustrated in Fig. 14b. Despite the low light condition of the fluorescence imaging process and the lack of contrast enhancement pre-processing, the multi-core segmentation performed perfectly with a rate of 100% of successful segmentation over all detected positions and produced precisely the measurements of the object found at each detected position. By combining the detection and the segmentation modules, the localizer provided 60.19% in terms of successful core recognition with no error. The estimation of the grid deformation also yielded satisfactory result : the row and column coordinates of all recognized cores during the localization task were accurately computed. Moreover, the final de-arraying outcome reached an overall accuracy of 92.56% – corresponding to a gain of 32.37% comparing to the localization phase. The improvement between the two phases of the de-arraying procedure obtained on fluorescence images is remarkably higher than those obtained on bright field images. It highlights the difference between the two imaging modes but also illustrates the impact of the segmentation algorithm on the performance of the proposed approach in the case of fluorescence images.

The majority of the time computing is spent on the detection task to compute the wavelet transform. Overall, the computational cost is less than 5 seconds for de-arraying a 1000×1000 image. The experiments were performed on a Macbook Pro equipped with 2.7 Ghz Intel Core i7, 16 Gb of RAM and the Mac OS X v. 10.12.4 operating system. The algorithm was implemented in Matlab and we exploited the intrinsic parallelism of the CPU by performing many ellipse-based segmentation in parallel.

4 Conclusion

This paper introduced a fast and efficient algorithm for de-arraying TMA by combining wavelet transform, active contour and thin-plate interpolation. The proposed ATMAD algorithm is adapted not only for bright field images but also for fluorescence images which are more challenging in terms of tissue localization due to complex backgrounds. This difficulty is carried out by a two-step approach : a fast detection followed by a careful segmentation to reduce the number of false alarms. The row and column coordinates of each localized tissue core are next computed by estimating the deformation of the design grid. Using the estimation of the deformation, tissue cores which are missed during localization can be later recognized and it refine thus the de-arraying result.

Acknowledgements

We would like to show our gratitude to Dr Jinhai Wang (Queen's University Belfast, Belfast, United Kingdom) and the AIDS and Cancer Specimen Resource Digital Library (University of California San Francisco) for sharing their valuable tissue microarray images which were used to evaluate the proposed approach.

Références

[1] H Battifora. The multitumor (sausage) tissue block : novel method for immunohistochemical antibody testing. *Lab Invest*, 55(2) :244–248, 1986.

[2] W H Wan, M B Fortuna, and P Furmanski. A rapid and efficient method for testing immunohistochemical reactivity of monoclonal antibodies against multiple tissue samples simultaneously. *J Immunol Methods*, 103 :121–129, 1987.

[3] H Battifora and P Mehta. The checkerboard tissue block. An improved multitissue control block. *Lab Invest*, 63 :722âĂŞ724, 1990.

[4] J Kononen, L Bubendorf, A Kallionimeni, M Bärlund, P Schraml, S Leighton, J Torhorst, M J Mihatsch, G Sauter, and O P Kallionimeni. Tissue microarrays for high-throughput molecular profiling of tumor specimens. *Nat Med*, 4 :844–847, 1998.

[5] C E Gillett, R J Springall, D M Barnes, and A M Hanby. Multiple tissue core arrays in histopathology research : a validation study. *J Pathol*, 192 :549âĂŞ553, 2000.

[6] J K Chan, C S Wong, W T Ku, and M Y Kwan. Reflections on the use of controls in immunohistochemistry and proposal for application of a multitissue spring-roll control block. *Ann Diagn Pathol*, 5 :329âĂŞ336, 2000.

[7] M Schoenberg Fezjo and D J Slamon. Frozen tumor tissue microarray technology for analysis of tumor RNA, DNA and proteins. *J Pathol*, 150 :1645âĂŞ1650, 2001.

[8] J Packeisen, H Buerger, R Krech, and W Boecker. Tissue microarrays : a new approach for quality control in immunohistochemistry. *J Clin Pathol*, 55 :613âĂŞ615, 2002.

[9] S Badve, C Deshpande, Z Hua, and L Lögdberg. Expression of invariant chain (CD 74) and major histocompatibility complex (MHC) class II antigens in the human fetus. *J Histochem Cytochem*, 50 :473âĂŞ482, 2002.

[10] A Hidalgo, P Piña, G Guerrero, M Lazos, and M Salcedo. A simple method for the construction of small format tissue arrays. *J Clin Pathol*, 56 :144âĂŞ146, 2003.

[11] L Wang, M T Deavers, A Malpica, E J Silva, and J Liu. Tissue macroarray : a simple and cost-effective method for high-throughput studies. *Appl Immunohistochem Mol Morphol*, 11 :174âĂŞ176, 2003.

[12] H L Dan, Y L Zhang, Y Zhang, Y D Wang, Z S Lai, Y J Yang, H H Cui, Y T Jian, J Geng, Y Q Ding, C H Guo, and D Y Zhou. A novel method for preparation of tissue microarray. *World J Gastroenterol*, 10 :579âĂŞ582, 2004.

[13] C H Pan and H Chen, C ans Chiang. An easy method for manual construction of high-density tissue arrays. *Appl Immunohistochem Mol Morphol*, 12 :370âĂŞ372, 2004.

[14] M Datta, A Kahler, V Macias, T Brodzeller, and A Kajdacsy-Balla. A simple inexpensive method for the production of tissue microarrays from needle biopsy specimens : examples with prostate cancer. *Appl Immunohistochem Mol Morphol*, 13 :96âĂŞ103, 2005.

[15] K Montgomery, S Zhao, M van de Rijn, and Y Natkunam. A novel method for making "tissue" microarrays from small numbers of suspension cells. *Appl Immunohistochem Mol Morphol*, 13 :80âĂŞ84, 2005.

[16] D Pilla, F M Bosisio, R Marotta, S Faggi, P Forlani, M Falavigna, I Biunno, E Martella, P De Blasio, S Borghesi, and G Cattoretti. Tissue microarray design and construction for scientific, industrial and diagnostic use. *J Pathol Inform*, 3, 2012.

[17] H Vrolijk, W Sloos, W Mesker, P Franken, R Fodde, H Morreau, and H Tanke. Automated acquisition of stained tissue microarrays for high-throughput evaluation of molecular targets. *J Mol Diagn*, 5(3) :160–167, 2003.

[18] W Chen, M Reiss, and D J Foran. A prototype for unsupervised analysis of tissue microarrays for cancer research and diagnostics. *IEEE Trans Inform Technol Biomed*, 8(2) :89–96, 2004.

[19] R DellâĂŹAnna, F Demichelis, M Barbareschi, and A Sboner. An automated procedure to properly handle digital images in large scale tissue microarray experiments. *Comput Methods Programs Biomed*, 79 :197–208, 2005.

[20] A Rabinovich, S Krajewski, M Krajewska, A Shabaik, S M Hewitt, S Belongie, J C Reed, and J H Price. Framework for parsing, visualizing and scoring tissue microarray images. *IEEE Trans Inform Technol Biomed*, 10(2) :209–219, 2006.

[21] B Lahrmann, N Halama, K Westphal, C Ernst, Z Elsawaf, P Sinn, F X Bosch, H Dickhaus, D Jäger, P Schirmacher, and N Grabe. Robust gridding of TMAs after whole-slide imaging using template matching. *Cytometry A*, 77(12) :1169–1176, 2010.

[22] Y Wang, K Savage, C Grills, A McCavigan, J A James, D A Fennell, and P W Hamilton. A TMA de-arraying method for high throughput biomarker discovery in tissue research. *PLoS ONE*, 6(6) :e26007, 2011.

[23] J L Starck and R Murtagh. Image restoration with noise suppression using wavelet transform. *Astronomy and Astrophysics*, 288 :342–348, 1994.

[24] P ThÃľvenaz, R Delgado-Gonzalo, and M Unser. The ovuscule. *IEEE Trans Pattern Analysis Machine Intelligence*, 33(2) :382–393, 2011.

[25] F L Bookstein. Principal warps : thin-plate splines and the decomposition of deformationa. *IEEE Trans Pattern Analysis Machine Intelligence*, 11(6) :567–585, 1989.

[26] C Kervrann, C O Sorzano, S T Acton, J C Olivo-Marin, and M Unser. A guided tour of selected image processing and analysis methods for fluorescence and electron microscopy. *IEEE J Selected Topics Signal Processing*, 10(1) :6–30, 2016.

[27] E J Breen, G H Joss, and K L Williams. Locating objects of interest within biological images : The top hat box filter. *Computer Assisted Microscopy*, 3(2) :97âĂŞ102, 1991.

[28] J C Olivo-Marin. Extraction of spots in biological images using multiscale products. *Pattern Recognition*, 35(9) :1989–1996, 2002.

[29] D Sage, F R Neumann, F Hediger, S M Gasser, and M Unser. Automatic tracking of individual fluorescence particles : Application to thestudy of chromosome dynamics. *IEEE Trans Image Processing*, 14(9) :1372âĂŞ1383, 2005.

[30] B Zhang, M J Fadili, J L Starck, and J C Olivo-Marin. Multiscale variance-stabilizing transform for mixed-Poisson-Gaussian processes and its applications in bioimaging. *Proc IEEE Intl Conf Image Processing*, 6 :233–236, 2007.

[31] I Smal, W Niessen, and E Meijering. A new detection scheme for multiple object tracking in fluorescence microscopy by joint probabilistic data association filtering. *Proc IEEE Intl Symp Biomed Imaging*, page 264âĂŞ267, 2008.

[32] A Basset, J Boulanger, P Bouthemy, C Kervrann, and J Salamero. SLT-LoG : A vesicle segmentation method with automatic scale selection and local thresholding applied to TIRF microscopy. *Proc IEEE Intl Symp Biomed Imaging*, pages 533–536, 2014.

[33] Z Püspöki, J P Ward, D Sage, and Unser M. Fast detection and refined scale estimation using complex isotropic wavelets. *Proc IEEE Intl Symp Biomed Imaging*, pages 512–515, 2015.

[34] Z PÃijspÃűki, D Sage, J P Ward, and Unser M. Spotcaliper : fast wavelet-based spot detection with accurate size estimation. *Bioinformatics*, 32(8) :1278–1280, 2016.

[35] M Kass, A Witkin, and D Terzopoulos. Snakes : Active contour models. *Intl J Computer Vision*, 1(4) :321–331, 1998.

[36] R Delgado-Gonzalo, V Uhlmann, D Schmitter, and M Unser. Snakes on a plane : A perfect snap for bioimage analysis. *IEEE Signal Processing Mag*, 32(1) :41–48, 2015.

[37] S Zhu and A Yuille. Region competition : unifying snakes, region growing, energy/Bayes/MLD for multiband image segmentation. *IEEE Trans Pattern Analysis Machine Intelligence*, 18(9) :884–890, 1996.

[38] T F Chan and L Vese. Active contoru without edges. *IEEE Trans Image Processing*, 10(2) :266–277, 2001.

[39] C Kervrann and A Trubuil. Optimal level curves and minimizers of cost functionals in image segmentation. *J Mathematical Imaging and Vision*, 17(2) :153–174, 2002.

[40] V Caselles, R Kimmel, and G Sapiro. Geodesic active contours. *Intl J Computer Vision*, 22(1) :61–79, 1997.

[41] A Yuille, P W Hallinan, and D S Cohen. Feature extraction from faces using deformable templates. *Intl J Computer Vision*, 8(2) :99–111, 1992.

[42] Y Amit, U Grenander, and M Piccioni. Structural image restoration through deformable templates. *J Am Statist Assoc*, 86 :376–387, 1991.

[43] U Grenander, Y Chow, and D M Keenan. *Hands – A Pattern Theoretic Study of Biological Shapes*. Springer-Verlag, Berlin/Heidelberg/New-York, 1991.

[44] U Grenander and M Miller. Representations of knowledge in complex systems. *J Royal Statistical Society, series B*, 56(4) :549–603, 1994.

[45] C Kervrann and F Heitz. A hierarchical Markov modeling approach for the segmentation and tracking of deformable shapes. *Graphical Models and Image Understanding*, 60(3) :173–195, 1998.

[46] X Descombes. *Stochastic Geometry for Image Analysis*. Wiley-ISTE, 978-1-84821-240-4, 2011.

[47] T F Cootes, C J Taylor, D H Cooper, and J Graham. Active shape models - their training and application. *CVGIP : Image Understanding*, 61 :38–59, 1994.

[48] L H Staib and J S Duncan. Boundary finding with parametrically deformable models. *IEEE Trans Pattern Analysis Machine Intelligence*, 14(11) :1061–1075, 1992.

[49] P ThÃľvenaz and M Unser. Snakuscules. *IEEE Trans Image Processing*, 17(4) :585–593, 2008.

[50] X Descombes. Multiple objects detection in biological images using a marked point process framework. *Methods*, 115 :2–8, 2016.

[51] A K Pediredla and C S Seelamantula. A unified approach for optimization of snakuscules and ovuscules. *Proc IEEE Intl Conf Acoustics, Speech, and Signal Processing*, pages 681–684, 2012.

[52] F OâĂŹSullivan and Q Qian. A regularized contrast statistic for object boundary estimation âĂŞ implementation and statistical evaluation. *IEEE Trans Pattern Analysis Machine Intelligence*, 16(6) :561–570, 1994.

[53] S Mallat. *A Wavelet Tour of Signal Processing (third edition : The Sparse Way)*. Academic Press, Boston, 2008.

[54] J-L Starck and F Murtagh. *Astronomical Image and Data Analysis*. Springer-Verlag, 978-3-540-33025-7, 2002.

[55] J-L Starck, J Fadili, and F Murtagh. The undecimated wavelet decomposition and its reconstruction. *IEEE Trans Image Processing*, 16(2) :297–309, 2007.

Appendixes

A.1 Isotropic wavelet frame

Mathematically, a wavelet $\psi : \mathbb{R}^d \longrightarrow \mathbb{R}$ is a function of zero average :

$$\int \dots \int_{\mathbb{R}^d} \psi(\mathbf{x})\ d\mathbf{x} \ = \ 0 \ , \tag{32}$$

where d is the number of dimensions (usually, $d = 1,\ 2$ or 3). When the wavelet function ψ is isotropic (*i.e.* $\psi(-\mathbf{x}) = \psi(\mathbf{x}), \forall \mathbf{x} \in \mathbb{R}^d$), we deduce the wavelet atoms $\{\psi_{(\mathbf{t},s)}\}_{(\mathbf{t},s)\in\mathbb{R}^d\times\mathbb{R}_+^*}$ by dilation of ψ with factor s and translation by vector $\mathbf{t}$ as :

$$\psi_{(\mathbf{t},s)}(\mathbf{x}) = \frac{1}{s^d}\ \psi\left(\frac{1}{s}(\mathbf{x}-\mathbf{t})\right) \ . \tag{33}$$

The wavelet transform of a square-integrable function $u \in L^2(\mathbb{R}^d)$ is defined as the inner product (in $\mathbb{R}^d$) of u and the wavelet atom $\psi_{(\mathbf{t},s)}$ as following :

$$\Psi u(\mathbf{t},s) = \left\langle u, \psi_{(\mathbf{t},s)} \right\rangle = \int \dots \int_{\mathbb{R}^d} u(\mathbf{x})\ \bar{\psi}_{(\mathbf{t},s)}(\mathbf{x})\ d\mathbf{x} \ , \tag{34}$$

where $\bar{\psi}_{(\mathbf{t},s)}$ denotes the complex conjugate of $\psi_{(\mathbf{t},s)}$. To construct a shift invariance representation, we consider the dyadic wavelets derived by discretizing the scale parameter along a dyadic sequence $\{2^j\}_{j\in\mathbb{Z}}$, while the translation parameter is not sampled as :

$$\left\{\psi_j(\mathbf{x}) = \frac{1}{2^{dj}}\ \psi\left(\frac{\mathbf{x}}{2^j}\right)\right\}_{j\in\mathbb{Z}} \ . \tag{35}$$

The family $\{\psi_j\}_{j\in\mathbb{Z}}$ is a frame of $L^2(\mathbb{R}^d)$ according to [53]. Using this family, the isotropic wavelet transform of u at the scale (or resolution) 2^j and the position $\mathbf{x} \in \mathbb{R}^d$ is :

$$\begin{aligned} \Psi_j u(\mathbf{x}) &= \int \dots \int_{\mathbb{R}^d} u(\mathbf{x})\ \frac{1}{2^{dj}}\ \psi\left(\frac{1}{2^j}(\mathbf{x}-\mathbf{t})\right) d\mathbf{t} \\ &= u \star \check{\psi}_j(\mathbf{x}), \end{aligned} \tag{36}$$

where $\check{\psi}_j(\mathbf{x}) = \psi_j(-\mathbf{x}) = \psi_j(\mathbf{x})$ since ψ_j is isotropic. The wavelet coefficient $\Psi_j u(\mathbf{x})$ can also be expressed as the difference of approximations of u at subsequent scales as following :

$$\begin{aligned} \Psi_j u(\mathbf{x}) &= u_{j-1}(\mathbf{x}) - u_j(\mathbf{x}) \ , \\ u_j(\mathbf{x}) &= \chi_j \star u_{j-1}(\mathbf{x}) = \lim_{k\to+\infty} (\chi_j \star \dots \star \chi_{j-k}) \star u(\mathbf{x}), \end{aligned} \tag{37}$$

where u_j and χ_j denote respectively the approximation of u and the smoothing function at the scale 2^j.

The infinite convolution cascade $\phi_j = \lim_{k\to+\infty} (\chi_j \star \dots \star \chi_{j-k})$ represents the approximation operator applied on u at the given resolution 2^j. In order to favor the simplest computation of the convolution sequence in (38), the selection of $(\chi_j)_{j\in\mathbb{Z}}$ is critical. Among many function families, Gaussian functions are convenient since it satisfies the semi-group property (i.e. the convolution of two Gaussians is also a Gaussian with variance being the sum of the original variances) :

$$G_{\sigma_a} \star G_{\sigma_b}(\mathbf{x}) = G_{\sqrt{\sigma_a^2+\sigma_b^2}}(\mathbf{x}) \ , \tag{38}$$

where G_σ is a Gaussian with standard deviation σ.

Therefore, if we choose χ_j being a Gaussian G_{σ_j} with standard deviation σ_j, the convolution sequence $(\chi_j \star \dots \star \chi_{j-k})$ can be easily computed by summing $\sigma_j^2, \dots, \sigma_{j-k}^2$. Since resolution decreases by a factor 2 between two consecutive scales, it is appropriate to set $\sigma_j = 2\sigma_{j-1} = 2^{j-1}\sigma_1$, where σ_1 is a reference standard deviation according to the Shannon-Nyquist sampling step. Thus, we have :

$$\sum_{k=0}^{+\infty} \sigma_{j-k}^2 = \sum_{k=0}^{+\infty} \left(2^{j-k-1}\sigma_1\right)^2 = \frac{4^j}{3}\sigma_1^2 \ . \tag{39}$$

Then, the approximation operator at the scale 2^j can be expressed as a convolution with a Gaussian of variance $(4^j/3)\sigma_1^2$:

$$\phi_j(\mathbf{x}) = \lim_{k\to+\infty} (\chi_j \star \ldots \star \chi_{j-k})(\mathbf{x}) = G_{\sqrt{(4^j/3)\sigma_1^2}}(\mathbf{x}) \ . \tag{40}$$

Additionally, from equations (36) to (38), we deduce :

$$\psi(\mathbf{x}) = 2^{dj}(\phi_{j-1}(2^j\mathbf{x}) - \phi_j(2^j\mathbf{x})) = \phi_{-1}(\mathbf{x}) - \phi_0(\mathbf{x}) \ . \tag{41}$$

By generalizing the equation expressed the relation of the mother wavelet ψ and its associate scaling function ϕ as described in [54] as following :

$$\frac{1}{2^d}\psi\left(\frac{\mathbf{x}}{2}\right) = \phi(\mathbf{x}) - \frac{1}{2^d}\phi\left(\frac{\mathbf{x}}{2}\right), \tag{42}$$

a closed-form solution of the scaling function ϕ (also known as father wavelet) is obtained as :

$$\phi(\mathbf{x}) = \phi_0(\mathbf{x}) = G_{\sigma_1/\sqrt{3}}(\mathbf{x}) = \frac{1}{(2\pi\sigma_1^2/3)^{d/2}} \exp\left(-\frac{3\|\mathbf{x}\|_2^2}{2\sigma_1^2}\right). \tag{43}$$

Since ϕ is Gaussian, ψ is defined as the difference of two Gaussians (DOG) with the first standard deviation equal to half of the second one. Given a value of σ_1 as input, the wavelet atoms ψ_j which are also DOGs are determined using the equations (35) and (41). Hence, a class of isotropic wavelets can be simply characterized by only one parameter.

A.2 Direct wavelet decomposition algorithm and reconstruction

Starck *et al.* proposed a method for performing the isotropic undecimated wavelet transform in [55]. This algorithm is called the Starlet transform. Like the standard undecimated wavelet transforms, the Starlet transform uses the *à trous* algorithm [23] which inserts zeros (holes) in the discrete convolution kernel at each iteration. This kernel is a low-pass filter derived from the normalized cardinal B-spline of order 3 :

$$\begin{aligned} h^{(1D)}[k] &= \frac{1}{16}[1,\ 4,\ 6,\ 4,\ 1], \quad k \in \{-2,-1,0,1,2\}, \\ B_3(u) &= \frac{1}{12}(|u-2|^3 - 4|u-1|^3 + 6|u|^3 \\ &\qquad - 4|u+1|^3 + |u+2|^3). \end{aligned}$$

Yet, as the order tends to infinite, the normalized cardinal B-spline tend to a Gaussian function The kernel used for wavelet decomposition is then an approximation of a Gaussian. To avoid the decimation at each level, the insertion of holes in the kernel leads to approximation errors, since the kernels with holes are far from their corresponding scaling functions. The error cumulation through iterations increases with the level of the decomposition. In addition, the iterative convolution process involves the dependence of the higher level of the decomposition on its previous levels. To sum up, the limits of *à trous* algorithm are its inaccuracy and computational cost.

To overcome these limits, the discrete wavelet decomposition of a function u at the desired scale 2^j can be obtained by performing the discrete convolution between u and the corresponding wavelet atom ψ_j. In practice, since all computations are performed over discrete signals, the input signal is not u but its discrete approximation counterpart. Without losing the generality, one can assume this approximation is u_0. In fact, using (37) and (38), we have :

$$\begin{aligned} \Psi_j u(\mathbf{x}) &= u_{j-1}(\mathbf{x}) - u_j(\mathbf{x}) \\ &= \begin{cases} (\chi_{j-1} * \ldots \star \chi_1 - \chi_j \star \ldots \star \chi_1) \star u_0(\mathbf{x}) \text{ if } j > 1 \\ u_0(\mathbf{x}) - \chi_1 \star u_0(\mathbf{x}) \text{ if } j = 1 \end{cases} \\ &= (\phi_{j-1}^0 - \phi_j^0) \star u_0(\mathbf{x}) \\ &= \psi_j^0 \star u_0(\mathbf{x}), \end{aligned} \tag{44}$$

Level (j)	**Std. of** χ_j (σ_j)	**Variance of** ϕ_j^0 (v_j^2)
1	σ_1	σ_1^2
2	$2\sigma_1$	$5\sigma_1^2$
3	$4\sigma_1$	$21\sigma_1^2$
4	$8\sigma_1$	$85\sigma_1^2$
5	$16\sigma_1$	$341\sigma_1^2$
6	$32\sigma_1$	$1365\sigma_1^2$

TABLE 1 – Computation of the variance of the scaling function ϕ_j^0 at first few levels.

$$\text{where} \quad \phi_j^0 = \begin{cases} \chi_j \star \ldots \star \chi_1 & \text{if } j > 1, \\ \delta & \text{if } j = 1. \end{cases}$$

The key idea of our method is the computation of the scaling function ϕ_j^0 which results the convolution sequence $\chi_j \star \ldots \star \chi_1$. Since χ_j is chosen as a Gaussian with variance $\sigma_j^2 = 4^{j-1}\sigma_1^2$, the function of interest ϕ_j^0 is also a Gaussian with variance :

$$v_j^2 = \begin{cases} \displaystyle\sum_{k=1}^{j} 4^{k-1}\sigma_1^2 & \text{if } j \geq 1, \\ 0 & \text{if } j = 0. \end{cases} \tag{45}$$

The values of v_j^2 at first few levels are reported in the Table 1.

Hence, there are two ways to compute $\Psi_j u$. The fastest way is to compute directly the wavelet atom $\psi_j^0(\mathbf{x}) = \phi_{j-1}^0(\mathbf{x}) - \phi_j^0(\mathbf{x}) = G_{v_{j-1}}(\mathbf{x}) - G_{v_j}(\mathbf{x})$ (with convention $G_0(\mathbf{x}) = \delta(\mathbf{x})$). Then, the wavelet decomposition map is the convolution product $\Psi_j u(\mathbf{x}) = \psi_j^0 \star u_0(\mathbf{x})$. The alternative way is to compute two convolutions $u_{j-1}(\mathbf{x}) = \phi_{j-1}^0 \star u_0(\mathbf{x})$ and $u_j(\mathbf{x}) = \phi_j^0 \star u_0(\mathbf{x})$, thus the wavelet decomposition is derived by taking the difference of two computed results. This way is slower than the first one but it is useful to reconstruct the input signal u_0.

By construction, for any given level j, the formula of reconstruction of u_0 is :

$$\begin{aligned} u_0(\mathbf{x}) &= \sum_{k=1}^{j} \Psi u_k(\mathbf{x}) + u_j(\mathbf{x}) \\ &= \sum_{k=1}^{j-1} (u_{k-1} - u_k)(\mathbf{x}) + \Psi_j u(\mathbf{x}) + u_j(\mathbf{x}) \\ &= u_0(\mathbf{x}) - u_{j-1}(\mathbf{x}) + \Psi_j u(\mathbf{x}) + u_j(\mathbf{x}). \end{aligned} \tag{46}$$

The perfect reconstruction of u_0 is therefore possible if $u_0 - u_{j-1}$ and u_j are known. Yet, u_{j-1} and u_j are computed by using the alternative way of the wavelet decomposition. Instead of returning only the wavelet decomposition $\Psi_j u$, $u_0 - u_{j-1}$ and u_j are also stored if the user needs to perform the reconstruction step. This approach can be extended for multi-scale reconstruction. In fact, if we have $(\Psi_j u)_{j \in J}$ where $J = \{j_1, j_2, \ldots, j_{|J|}\} \subset \mathbb{N}^*$, the reconstruction formula is written as :

$$u_0(\mathbf{x}) = \frac{1}{|J|} \sum_{k=1}^{|J|} (u_0 - u_{j_k - 1} + \Psi u_{j_k} + u_{j_k})(\mathbf{x}). \tag{47}$$

In practice, wavelet-based algorithms compute over a set of subsequent scales (i.e. $J = \{j_0, j_0 + 1, \ldots, j_0 +$

$|J|-1\}$). In this case, the reconstruction formula is therefore :

$$u_0(\mathbf{x}) = u_0(\mathbf{x}) - u_{j_0-1}(\mathbf{x}) + \sum_{k=0}^{|J|-1} \Psi u_{j_0+k}(\mathbf{x}) + u_{j_0+|J|-1}(\mathbf{x}). \tag{48}$$

A.3 Partial derivatives of the ellipse quadratic form

Let $\{\mathbf{x}_0, a, b, \theta\}$ be the parameters of the ellipse Γ where $\mathbf{x}_0 = (x_0, y_0)$ is the center, a and b are the semi major and minor axes, and θ is the angle of rotation. We consider the quadratic form induced by Γ as :

$$\begin{aligned}
\|\mathbf{x}-\mathbf{x}_0\|_\Gamma^2 &= \left\| \begin{bmatrix} a^{-1} & 0 \\ 0 & b^{-1} \end{bmatrix} \begin{bmatrix} \cos\theta & \sin\theta \\ -\sin\theta & \cos\theta \end{bmatrix} (\mathbf{x}-\mathbf{x}_0) \right\|_2^2 \\
&= \left\| \begin{bmatrix} \dfrac{\cos\theta}{a} & \dfrac{\sin\theta}{a} \\ -\dfrac{\sin\theta}{b} & \dfrac{\cos\theta}{b} \end{bmatrix} (\mathbf{x}-\mathbf{x}_0) \right\|_2^2 \\
&= \left(\frac{\cos\theta}{a}(x-x_0) + \frac{\sin\theta}{a}(y-y_0)\right)^2 \\
&\qquad + \left(-\frac{\sin\theta}{b}(x-x_0) + \frac{\cos\theta}{b}(y-y_0)\right)^2 .
\end{aligned} \tag{49}$$

The partial derivatives of $\|\mathbf{x}-\mathbf{x}_0\|_\Gamma^2$ with respect to $\{\mathbf{x}_0, a, b, \theta\}$ are given by :

$$\begin{aligned}
\frac{\partial \|\mathbf{x}-\mathbf{x}_0\|_\Gamma^2}{\partial x_0} &= -2\left[\frac{\cos\theta}{a}\left(\frac{\cos\theta}{a}(x-x_0) + \frac{\sin\theta}{a}(y-y_0)\right)\right. \\
&\qquad \left. -\frac{\sin\theta}{b}\left(-\frac{\sin\theta}{b}(x-x_0) + \frac{\cos\theta}{b}(y-y_0)\right)\right]
\end{aligned} \tag{50}$$

$$\begin{aligned}
\frac{\partial \|\mathbf{x}-\mathbf{x}_0\|_\Gamma^2}{\partial y_0} &= -2\left[\frac{\sin\theta}{a}\left(\frac{\cos\theta}{a}(x-x_0) + \frac{\sin\theta}{a}(y-y_0)\right)\right. \\
&\qquad \left. +\frac{\cos\theta}{b}\left(-\frac{\sin\theta}{b}(x-x_0) + \frac{\cos\theta}{b}(y-y_0)\right)\right]
\end{aligned} \tag{51}$$

$$\frac{\partial \|\mathbf{x}-\mathbf{x}_0\|_\Gamma^2}{\partial a} = -\frac{1}{a}\left(\frac{\cos\theta}{a}(x-x_0) + \frac{\sin\theta}{a}(y-y_0)\right)^2 \tag{52}$$

$$\frac{\partial \|\mathbf{x}-\mathbf{x}_0\|_\Gamma^2}{\partial b} = -\frac{1}{b}\left(-\frac{\sin\theta}{b}(x-x_0) + \frac{\cos\theta}{b}(y-y_0)\right)^2 \tag{53}$$

$$\begin{aligned}
\frac{\partial \|\mathbf{x}-\mathbf{x}_0\|_\Gamma^2}{\partial \theta} &= 2\left(\frac{b}{a}-\frac{a}{b}\right)\left(\frac{\cos\theta}{a}(x-x_0) + \frac{\sin\theta}{a}(y-y_0)\right) \\
&\qquad \times \left(-\frac{\sin\theta}{b}(x-x_0) + \frac{\cos\theta}{b}(y-y_0)\right).
\end{aligned} \tag{54}$$